

Microstructure and Water Absorption of Ancient Concrete from Pompeii: An Integrated Synchrotron Microtomography and Neutron Radiography Characterization

Ke Xu ^{a,b,*}, Anton S. Tremsin ^c, Jiaqi Li ^{a,*}, Daniela M. Ushizima ^{b,d}, Catherine A. Davy ^e, Amine Bouterf ^f, Ying Tsun Su ^a, Milena Marroccoli ^g, Anna Maria Mauro ^h, Massimo Osanna ⁱ, Antonio Telesca ^g, Paulo J. M. Monteiro ^a

^a Department of Civil and Environmental Engineering, University of California, Berkeley, CA, 94720, USA

^b Computational Research Division, Lawrence Berkeley National Laboratory, Berkeley, CA, 94720, USA

^c Space Sciences Laboratory, University of California, Berkeley, CA, 94720, USA

^d Berkeley Institute of Data Science, University of California, Berkeley, CA, 94720, USA

^e Univ. Lille, CNRS, Centrale Lille, ENSCL, Univ. Artois, UMR 8181 - UCCS - Unité de Catalyse et de Chimie du Solide, Lille F-59000, France

^f Laboratoire de Mécanique et Technologie (LMT), ENS Paris-Saclay, CNRS Université Paris-Saclay, Cachan Cedex, 94235, France

^g Department of Environmental Engineering and Physics, School of Engineering, University of Basilicata, Potenza 85100, Italy

^h Head of research and innovation area of Archeological Park of Pompeii, via Plinio 4, Pompeii, NA, 80045, Italy

ⁱ General Director of Archeological Park of Pompeii, via Plinio 4, Pompeii, NA, 80045, Italy

* Corresponding authors.

E-mail addresses:

Ke Xu: ke_xu@berkeley.edu

Jiaqi Li: jiaqi.li@berkeley.edu

Abstract

There is renewed interest in using advanced techniques to characterize ancient Roman concrete. In the present work, samples were drilled from the “Hospitium” in Pompeii and were analyzed by synchrotron microtomography (μ CT) and neutron radiography to study how the microstructure, including the presence of induced cracks, affects their water adsorption. The water distribution and absorptivity were quantified by neutron radiography. The 3D crack propagation, pore size distribution and orientation, tortuosity, and connectivity were analyzed from μ CT results using advanced imaging methods. The concrete characterization also included classical methods (e.g., differential thermal–thermogravimetric, X-ray diffractometry, and scanning electron microscopy). Ductile fracture patterns were observed once cracks were introduced. When compared to Portland cement mortar/concrete, Pompeii samples had relatively high porosity, low connectivity, and similar coefficient of capillary penetration. In addition, the permeability was predicted from models based on percolation theory and the pore structure data to evaluate the fluid transport properties.

Key Words

Roman concrete; Neutron radiography; Synchrotron microtomography; Image analysis (B);

Fracture; Pore structure; Transport Properties (C)

1. Introduction

The desire to extend the life cycle of the modern concrete infrastructure and to reduce its lifespan carbon footprint have instigated a renewed interest in determining the reasons for the long-term durability of ancient Roman concrete. State-of-the-art techniques, developed to study high-performance materials, have been recently applied to various ancient Roman concrete samples. Synchrotron radiation methods have been particularly successful in providing new insights into the complex micro and nanostructure of ancient Roman concrete. The use of high-pressure x-ray diffraction has given information about the mechanical behavior of Al-tobermorite that forms in ancient Roman seawater concrete, while soft x-ray nanotomography allowed for the mathematical morphology quantification of the cluster of these Al-tobermorite nanocrystals [1]. Jackson et al. [2] produced a seminal work on the formation of phillipsite and Al-tobermorite using x-ray microdiffraction. Scanning transmission X-ray microscopy (STXM) proved to be a powerful tool to understand the nanoscale bonding environments of Al and Si in Al-tobermorite and C-A-S-H [3]. Using synchrotron high-resolution x-ray diffraction (XRD), Vanorio and Kanitpanyacharoen [4] formulated a ground-breaking hypothesis that the caprock of the Campi Flegrei Caldera has a similar fibrous microstructure to the existing ancient Roman concrete formed by the lime-pozzolanic reactions. Recently, Palomo et al. [5] published a critical evaluation of the current developments in the characterization of ancient Roman concrete and how it can contribute to the new generation of green hybrid cement.

There is a consensus that the lack of concrete durability is associated with the penetration of water, often containing deleterious species. This deterioration is exacerbated by the presence of cracks,

which provide a faster pathway to the ingress of water. Jackson et al. [6] studied the crack resistance and resilience in Imperial Roman architectural mortar, but there is a lack of detailed information on the effect of the microstructure, particularly the effects of cracks on the concrete water ingress. The purpose of the present paper is to provide quantitative data on the dynamics of water absorption by uncracked and cracked samples from Pompeii using neutron radiography. The unique capability of neutron imaging to map water distribution within concrete samples is enabled by the relatively high neutron attenuation cross-section by hydrogen [7, 8], with relatively low absorption by the concrete itself. The integration of X-ray microtomography and neutron imaging, implemented in this study, allowed a systematic investigation of how concrete microstructure affects the dynamics of water penetration in Pompeii concrete samples. The complex topology of the phases was determined by synchrotron X-ray microtomography (μ CT). The extracted samples did not show any cracks, so after the μ CT scans, cracks were introduced by loading and the samples were retested to measure the influence of cracks on the fluid flow. Due to the complexity of the microstructure, it was necessary to improve the existing segmentation methods for the 3D tomographic images. While a separate publication will describe the intricacies of the proposed methodology, here, a short description will be given in section 2 for the benefit of the interested reader.

2. Samples and experimental methods

Nowadays, approximately 49 of the 66 hectares of Pompeii have been excavated. In 1858, the Archeologist Giuseppe Fiorelli [9] divided the city into “regions” (neighborhoods) and “insulae” (blocks), see Fig. 1. The present work studies the Hospitium building (Figure 2a) located at Stabiana street n.3 (Figure 2b), near the Stabiae gate in insula 1 of Regio I (Figure 2b). In the East

side part of Stabiana street, with the exception of very few accommodations, there was an almost uninterrupted series of tabernae hospitia, cauponae, stabula and officinae. The Hospitium building, excavated in 1872, has an area of about 600 square meters and it is delimited to the North by a shop (street n.4), to the South by an old “popina” (Roman wine bar/tavern frequented by the lower classes and slaves, where a limited menu of simple foods and wines was available, street n. 2), to the East by «Via Stabiana» and to the West by a non-paved alley. The ground floor had a big stable and a spacious «latrina»; the first floor, probably accessible through a staircase, was covered and composed only by bedrooms.

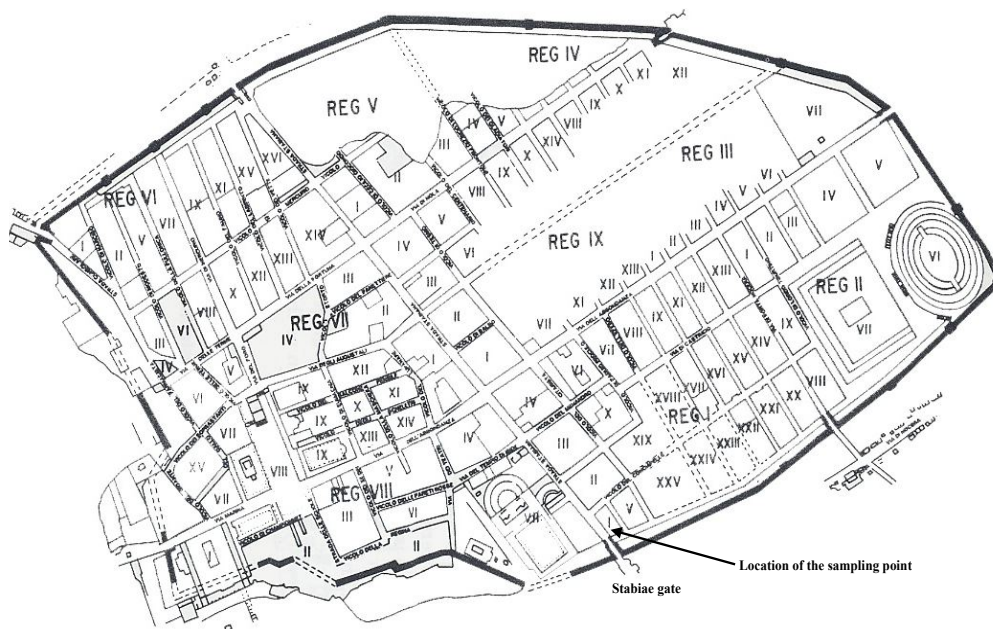


Figure 1. Plan of Pompeii with the location of the sample extraction.

All mortar samples were carefully collected at a depth of about 50 mm on both lateral sides of the building walls and pillars for avoiding weathering of any type, as well as a sampling of the powder deposited on the surfaces after the collapse. A small core drill was employed for extracting larger

samples from the walls of the house, and both a hammer and a small chisel were used for collecting the bedding mortars between bricks.



Figure 2. Photographs of (a) Hospitium entrance and (b) Via Stabiana.

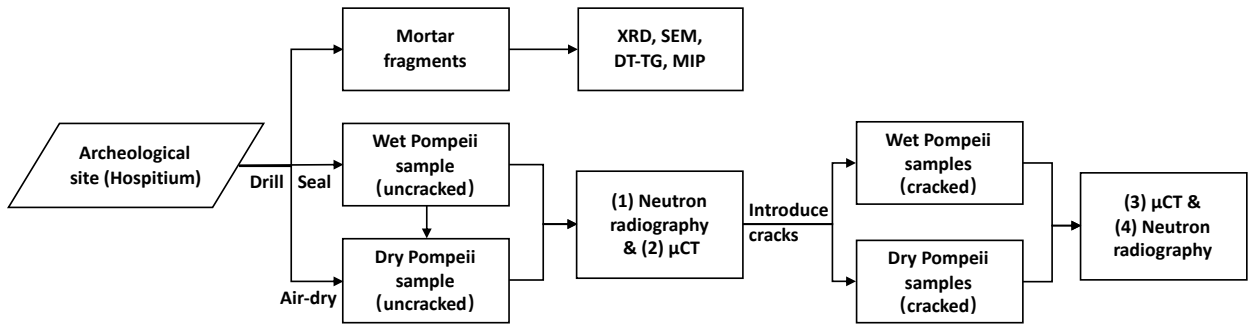


Figure 3. A schematic diagram of the experimental workflow for the study of Ancient Concrete from Pompeii.

A series of experiments (see Fig.3) was conducted to systematically investigate the microstructure and water transport mechanism in these mortar samples. The numbers indicate the sequence of the experiments, and detailed information about each experiment is described in the following sections.

2.1 XRD, SEM, DT-TG and MIP analysis

A large number of mortar fragments were investigated with scanning electron microscopes (SEM) and Mercury intrusion porosimetry (MIP); other fragments were first crushed with a pestle in an agate mortar, and the obtained pieces, composed by both aggregate and binder, were manually separated. The binder fraction was further ground to pass a 90 μm sieve and then tested by X-ray diffraction (XRD) and differential thermal–thermogravimetric (DT-TG) analyses. Three specimens were measured for each test. Simultaneously, DT–TG analysis was carried out in a Netzsch Tasc 414/3 apparatus operating in air atmosphere in the temperature range 20°–900 °C at a heating rate of 10 °C min^{-1} ; a sample mass equal to 100 mg was placed inside a 150 μL alumina top-opened crucible.

XRD analysis was employed for the determination of pulverized samples mineralogical composition. It was performed with a BRUKER D2 PHASER (Solex detector, Cu $K\alpha$ radiation, and 0.02°2 θs^{-1} scanning rate) equipped with an EVA software for the evaluation of the spectra. Peak intensity was measured and expressed in counts per second. The sample morphology was inspected with a Zeiss Supra 40 SEM (3-15 kV, voltage; 500 pA–2 nA, current intensity). Specimens were gold-coated using an EMITECK 950 apparatus. An energy-dispersive X-ray spectrometer (EDS) was employed to evaluate qualitatively the chemical composition of the areas of interest [10].

The porosity measurements were performed using a Thermo- Finnigan Pascal 240 Series Mercury Porosimeter (maximum pressure, 200 MPa) equipped with a low-pressure unit (140 Series) able

to generate a high vacuum level (10 Pa) and operate between 100 and 400 kPa. With increasing pressure, mercury is gradually able to penetrate the bulk sample volume. If the pore system is composed of an interconnected network of capillary pores in communication with the outside of the sample, mercury enters the smallest pore neck at a corresponding pressure value. If the pore system is discontinuous, mercury may penetrate the sample volume provided that its pressure is sufficient to break through pore walls. In any case, the pore width related to the highest rate of mercury intrusion per change in pressure is known as the “critical” or “threshold” pore width [11], which represents the lowest width of pore necks connecting a continuous system. A unimodal or multimodal pore size distribution can be obtained, depending on the occurrence of one or more peaks in the derivative volume plot.

2.2 Neutron radiography and water (capillary) absorption experiments

Two concrete samples from the same location in Hospitium, Pompeii with dimensions of $23.5 \times 27.6 \times 27.6 \text{ mm}^3$ and $17.8 \times 23.0 \times 27.5 \text{ mm}^3$ were studied. Sample DP was air-dried after drilled from the Hospitium which is located along Via Stabiana, Pompeii, while sample WP was originally wet and was sealed after drilling to analyze the original water distribution in ancient Roman concrete. For air-drying condition, the sample was kept under vacuum in a desiccator containing silica gel and soda lime to ensure protection against H_2O and CO_2 . First, both samples (Fig. 4 (a) and (b)) were scanned using neutron radiography and synchrotron microtomography to analyze the water distribution, water absorption, and microstructure at the original state (uncracked state). After these measurements, cracks were introduced into both samples by applying uniaxial compressive stresses. Finally, both samples (Fig. 4 (c) and (d)) were scanned again using neutron

radiography and synchrotron microtomography to compare the water distribution, water absorption, and microstructure measured at original state with those obtained with cracked samples (cracked state).



(a) DP before cracking



(b) WP before cracking



(c) DP after cracking



(d) WP after cracking

Figure 4. Geometry and dimensions of two samples.

Neutron imaging experiments of DP and WP concrete samples from Pompeii were done at the Materials and Life Sciences (MLF) Facility at the Japan Proton Accelerator Research Complex J-PARC. The pulsed neutron beam at this spallation neutron source operating at 25 Hz neutron pulse frequency enabled the possibility to measure neutron transmission spectra in every pixel of the

images. More than 250,000 transmission spectra were measured in the experiments simultaneously, each within 55 μm pixel of 512x512 neutron counting detector. A fast neutron counting detector with Microchannel Plates (MCPs) and Timepix readout with an active area of 28x28 mm^2 , built at the University of California at Berkeley in collaboration with Nova Scientific, was used for the energy-resolved neutron radiography measurements [12-14].

The neutron Time of Flight (ToF) method was used to reconstruct the energy of each detected neutron, allowing transmission spectra to be measured simultaneously in a wide range of energies from epithermal ($\sim\text{eV}$ energy) neutrons to cold neutrons (meV energies). All measured spectra were normalized by the spectrum taken with no sample present in the beam to correct for the spectral features of the interrogating beam and the spatial non-uniformity of both the detector response and the neutron beam itself.

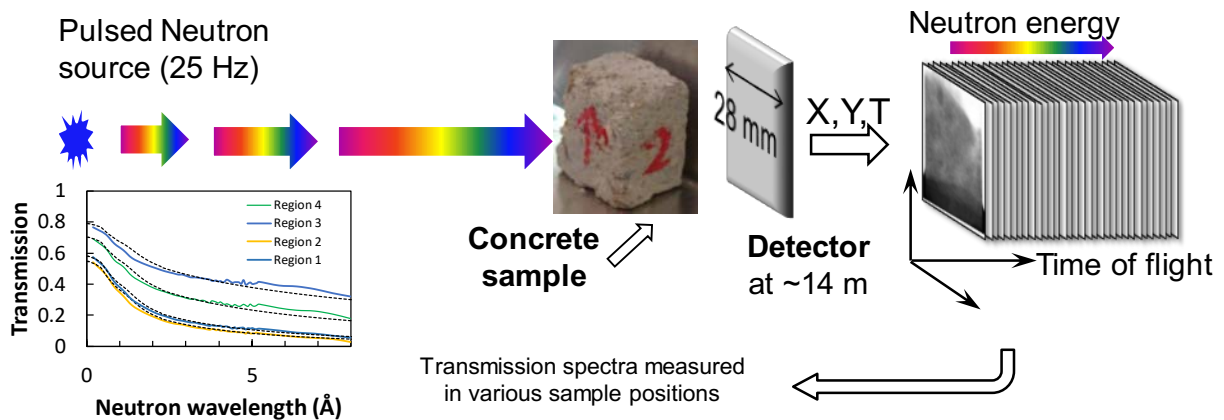


Figure 5. Schematic experimental setup of neutron energy-resolved imaging used for mapping the water distribution and dynamics of water penetration.

The analysis of these neutron transmission spectra allowed quantitative mapping of water distribution in as-extracted concrete samples (uncracked DP and WP) as well as investigation of the dynamics of water penetration in as-extracted and cracked samples (cracked DP and WP). More details on the reconstruction of water concentration in concrete samples are described in [13, 15]. The samples were placed 5-6 cm from the active area of the detector, which resulted in only a small fraction ($<2.5\%$) of neutrons scattered by water to reach the detector and introduced unwanted background signals. Because of that small contribution of scattered neutrons, no scatter rejection techniques were implemented in the present study. The accuracy of the water concentration mapping was verified with a calibration step wedge sample where the known thickness of water was reconstructed from the measured neutron transmission data [15].

The dynamics of water penetration was performed with a white spectrum beam in order to map the location of water in the sample on a sub-second time scale. Measurements of neutron transmission spectra in each pixel of the data set require relatively long integration (tens of minutes) in order to acquire sufficient statistics, while the dynamics of water absorption was studied with multiple images acquired per second. Water was introduced into the bottom part of an aluminum container, in which the concrete samples were placed in front of the detector, and consecutive transmission images were acquired multiple times per second. Thus, the location of the waterfront driven up into the sample by capillary forces was visualized as a sharp drop in sample transmission at the boundary of wetted and dry concrete samples.

2.3 Synchrotron X-ray microtomography experiments

Synchrotron μ CT was done at beamline 8.3.2 at the Advanced Light Source (ALS) of the Lawrence Berkeley National Laboratory [16]. A white beam was used in the experiment, where the X-ray beam needs to go through the concrete samples. The beam energy was set to 35 keV, which is adequate for the penetration of the specimens; the intensity is kept constant at 500 mA. During a scan, the sample was mounted on the circular holder and was rotated about an axis perpendicular to the horizontal plane over 180° , with total 1969 2D radiographs obtained. Each projection was acquired on a 2560px CCD camera (PCO.edge sCMOS) equipped with an 8.3 mm field of view and a 1x Mitutoyo magnification optical objective lens. To improve phase contrast and achieve a better image quality, an exposure time of 15 ms per projection was used to keep the transmission ratio of the beam below 40% based on the Beamline 8.3.2 Manual. The pixel resolution under these conditions was $9.5 \mu\text{m}$. After each scan, a 3D data volume (tomogram) was reconstructed from the 2D radiographs using TomoPy [17]. The custom Python scripts developed for ALS 8.3.2 based on TomoPy and used in this study can be found at <https://bitbucket.org/berkeleylab/als-microct-python/src>. More details of tomographic reconstruction are described elsewhere [18]. After the reconstruction, two stacks of tomograms for sample DP (uncracked and cracked states) with a dimension of $2560 \times 2560 \times 2324$ voxels³ (32-bit 56.7 GB for each stack) and two stacks of tomograms for sample WP (uncracked and cracked states) with dimensions of $2560 \times 2560 \times 2324$ voxels³ (32-bit 56.7 GB for each stack) were obtained for analysis.

2.4 Preprocessing, visualization and segmentation of tomography images

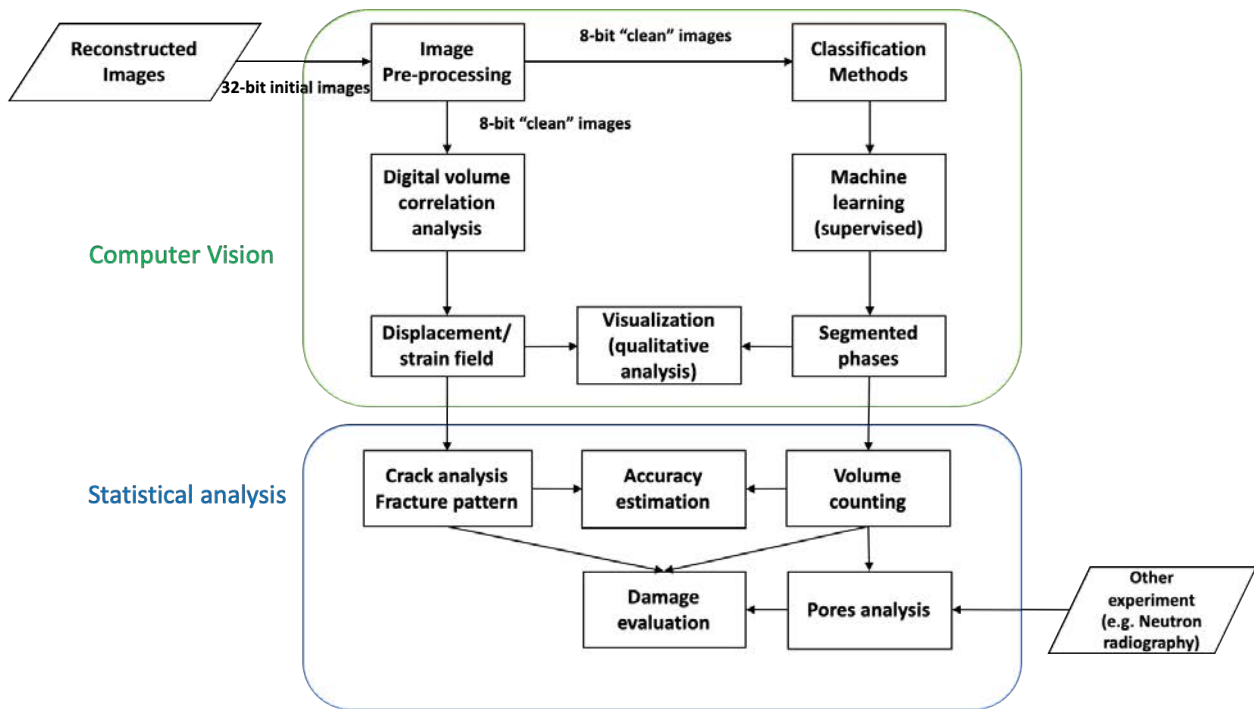


Figure 6. A schematic diagram showing the stages of computer vision and statistical analysis for tomography images

To conduct a systematic investigation of the sample microstructure and combine the neutron radiography images, we built a new pipeline (Fig. 6) for the autonomous and accurate μ CT image analysis. This pipeline contains two parts: computer vision and statistical analysis. In the computer vision analysis, preprocessed μ CT images were segmented into different phases using machine learning algorithms. The edge-preserving filters, mathematical morphology as well as an assortment of supervised machine learning algorithms, improved the segmentation accuracy when comparing to the traditional gray value threshold segmentation method. Meanwhile, advanced digital volume correlation (DVC) algorithms were performed on the preprocessed μ CT images of reference samples and deformed samples to calculate the displacement map and strain field. Both segmented 3D pore phase image and 3D principal strain field revealed the cracking propagation.

The DVC results also allow us to qualitatively verify the accuracy of phase segmentation. Then, qualitative and quantitative analysis was conducted based on 3D segmented phase images and strain fields. In addition, a comprehensive microstructure investigation was conducted combining neutron radiography and segmented images.

Image preprocessing was performed on Fiji [19], and this stage involves: a) transforming the slice images from 32-bit to 8-bit, b) removing the overlap (20 was set during the tile mode scans) of images between image stacks, c) removing the partial background and cropping out the region of interest (ROI), d) eliminating noise and ring artifacts from the images through the 3D bilateral filtering [20], and e) improving the contrast with a saturated pixel of 0.35. For DP and WP, two stacks of images could have different 3D rendering orientations and positions since the uncracked and cracked samples were scanned separately. The image volume registration method was applied to transform two stacks of images into one coordinate system for one sample. Translation transformation was used to preserve the same coordinate for the rotation centers of two stacks. Then, the cracked stack was rotated to keep the orientation of the bottom image slice in consistency with that of the uncracked stack, which reduced the rotation artifacts between scans.

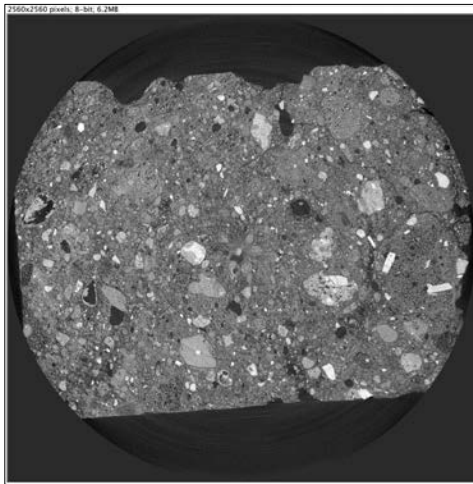
In this study, Tomviz [21] was used to visualize the reconstructed 3D μ CT images, segmented 3D μ CT images of different phases, and 3D crack evolutions from DVC. Dragonfly (Object Research Systems (ORS) Inc) was used to visualize the 3D connectivity of pore networks.

Image segmentation is the most crucial step for the quantitative analysis of 3D μ CT. To obtain the morphological representation of specific phase systems (e.g., the porous system in concrete) and

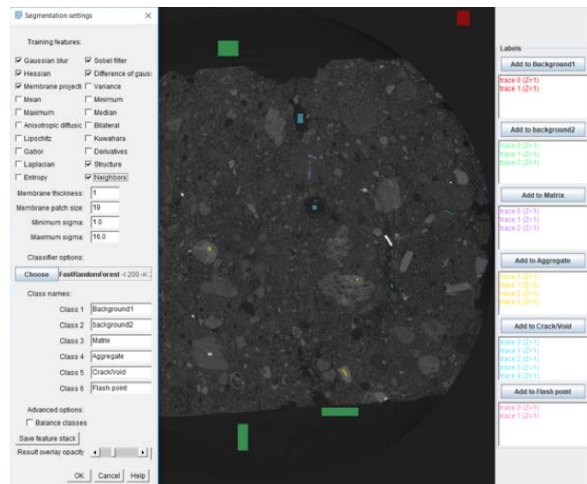
conduct further statistical analysis (e.g., intensity variation, porosity, size distribution, cross-section area, and network structure), a segmentation process is commonly implemented to separate images into discrete phases (e.g., pore phase, aggregate phase, and matrix phase in concrete). Local and global gray scale thresholding are the most commonly applied approaches for CT of concrete [22, 23]. The major drawback of these methods is to utilize one feature (i.e. grayscale in the images), and their accuracy and robustness are limited by the quality of the tomographic images [24, 25]. The segmentation results are unstable for the tomographic images, with low phase contrast, noise points, background regions, or attenuation problems.

Recently, machine learning (ML) algorithms have been successfully applied to the segmentation of structures with X-ray μ CT images of mineralogical samples. Shipman et al. [26] extracted quantitative mineralogical information regarding composition, porosity, and particle size of chromite ore samples. Camalan et al. [27] estimated the 2D-mineral map and its associated liberation spectrum of a particular chromite sample by using Random Forest Classification. These ML classifiers are robust, automatic, and multi-feature based. For the combination of extracting multiple image features from the raw data and applying ML image segmentation algorithms, Trainable Weka Segmentation Tool [19, 28] was used in this study. Considering both image segmentation accuracy and computing time, Grayscale, Mean, Median, Minimum, Maximum, Gaussian blur, Hessian, Anisotropic diffusion, and Difference of Gaussians were selected as the features for segmentation. At the same time, a small number of images were randomly selected from the whole data set as the training images. After feature selection, different regions (the most obvious objects corresponding to the target phases) in the training images were annotated as of target phases, which constructed the training data set.

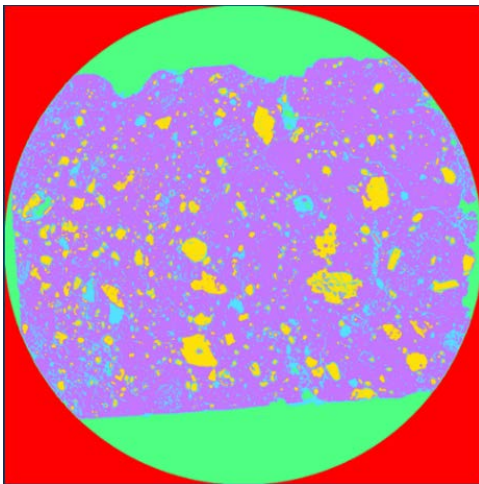
Five phases were separated from each other in the μ CT of concrete: background, supporting stage for the test, aggregate, matrix, and pore. Cracks were included in the pore phases. Different classifiers were trained using the selected features and training data set as a preliminary step. Based on the initial segmentation results on the training data set, more annotations were added to the misclassified regions, and the classifiers were re-trained and tuned until satisfactory segmentation results (testing pixel accuracy above 90% for each phase) were obtained. After training, the most suitable ML classifier was selected based on the segmentation results. The Random Forest Classifier, proposed by Tin Kam Ho [29], proved to have better performance compared with other ML classifiers (e.g., Linear perceptron classifier, SVM classifier, and Gaussian discriminant classifier) on our data set. Besides, the Random Forest algorithm has been one of the most accurate learning algorithms for μ CT segmentation and produces a highly accurate classifier for many CT image data sets [30]. Therefore, the Random Forest Classifier was selected and applied to the μ CT dataset of DP and WP samples. Figure 7 shows the segmentation procedures from a μ CT image to the segmented mask of the pore phase using the Random Forest Classifier. Table 1 shows the confusion matrices that highlight the accuracy in pixel classification results of the applied Random Forest model with inputs obtained from manually segmented samples (manual annotations). Note that both supporting and background phases were regarded as background phase in the construction of confusion matrices. Ushizima et al. [31] gave a detailed description of microstructure segmentation for ancient Roman concrete μ CT images.



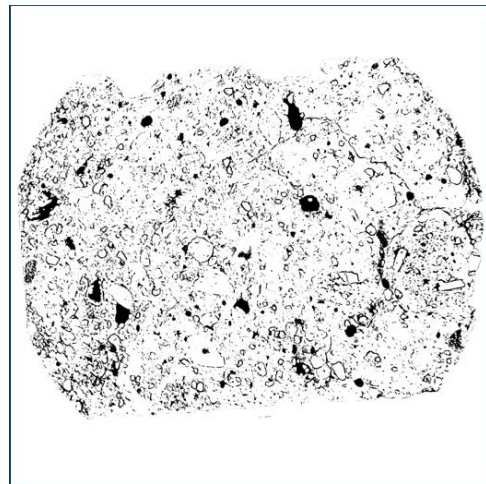
(a)



(b)



(c)



(d)

Figure 7. (a) Initial image, (b) feature selection and image annotations, (c) final classified image (Red phase: background, Green phase: supporting stage, Yellow phase: aggregate, Purple phase: matrix, Blue phase: pores), (d) segmentation of pores.

Table 1. Confusion matrix for sample DP and WP using Random Forest Classification.

%	Background	Aggregate	Matrix	Pore
Background	97.52	0	0	2.48
Aggregate	0	96.82	3.18	0
Matrix	0.01	0.17	98.43	1.39
Pore	0	0	5.21	94.79

2.5 Digital volume correlation

Separating intrinsic voids and introduced cracks with high accuracy in the 3D μ CT is challenging for image segmentation algorithms [32-34]. DVC is an appropriate image processing method to analyze the crack propagation without the distraction of intrinsic voids for the microtomography test. Roux et al. [35] calculated the displacement fields and evaluated the accuracy of the algorithm based on the analysis of an in-situ uniaxial compression CT test on a solid polypropylene foam. Bouterf et al. [36] analyzed the crack propagation and degradation mechanisms of lightweight plasterboard via a nail pull test conducted in-situ in a laboratory microtomography. In order to characterize the crack propagations from μ CT and its influence on the water absorption in the neutron radiography experiments, the digital volume correlation (DVC) method was applied for both qualitative understanding and quantitative evolution of complex 3D crack propagations in two samples. DVC techniques calculate the displacement field by minimizing the correlation residuals (i.e., the sum of squared grayscale differences between the reference volume and the deformed volume corrected by the calculated displacement field [36]) under the hypothesis of conservation of the grayscale of the analyzed microstructure of images. Then, the strain fields can be calculated from the displacement fields, and the crack propagation can be visualized and quantified [37, 38].

In this study, the displacement fields were measured when discretized over a finite element mesh made of 8-noded cubes (C8) [35]. Since the strains were small, a regularized approach was used [39, 40]. A steep displacement gradient indicated the presence of a crack, and the maximum equivalent strain was a measure of the crack opening displacement magnitude, which revealed the complex pattern of cracking more sensitively than the segmented pore images. The C8R developed on Matlab by Bouterf [41, 42], which used the regularized C8 element, was selected to conduct the DVC analysis for both DP and WP samples. Due to the limited storage of Matlab, the original reconstructed μ CT stacks ($2560 \times 2560 \times 2324$ voxels³) were scaled to $1280 \times 1280 \times 1162$ voxels³. For the mesh generation, the element size, which is comparable to the zone of interest (ZOI) size of classical Digital Image Correlation codes, was optimized to be $20 \times 20 \times 20$ voxels³ for global DVC to reduce the computational complexity and uncertainty, while still being able to capture complex displacements and micro cracks [39, 40]. The regularized lengths were set to be equal or larger than element size so that the high-frequency displacement fluctuations, which are not mechanically admissible, are filtered out.

2.6 Pore morphology and statistical analysis

3D pore network information is essential to assess the physicochemical properties of concrete, such as mechanical strength and permeability. 3D Pore morphology and statistical analysis were conducted on segmented pore phase images (binary images). More accurately, pore size distribution, porosity, pore area distribution along the Z-axis, aspect ratio, pore connectivity,

connectivity density, and tortuosity were characterized based on 3D segmented images of the pore phase.

3D discrete pore size distribution (DPSD) and continuous pore size distribution (CPSD) were computed [43]. DPSD is a simple measurement, where each pore object is considered as a sphere of identical volume to the original pore. DPSP is the relative pore volume as a function of the equivalent sphere diameter [43-45]. In comparison, the CPSD is based on the assumption that the pore network is a continuum and can be invaded by the fluid as in MIP [43]. In CPSD measurement, the pore objects (defined as spheres of identical volumes) are invaded from the largest pores to the smallest pores without the “ink bottle effect”. CPSD is defined as the relative volume of invaded spheres as a function of the sphere size [43]. In this paper, 3D DPSD and CPSD were performed by using Xlib plugin [43] in Fiji.

Porosity is defined as the percentage of pore voxels in the Volumes of Interest (VOI). The cross-section areas of the pores and cracks along the height (Z-axis) were calculated from 3D binary images of pore phase to associate the water absorption results from neutron radiography. Voxel connectivity analysis was performed based on a 6-connected voxel criterion, which means voxels are considered connected to form the “cluster/object” when the voxels share a common face with each other (pores are usually made of at least two voxels). Then, the pore objects (clusters) were used to characterize the aspect ratio, pore connectivity, and connectivity density.

To describe the morphology of pore objects in 3D, the aspect ratio (elongation) of each individual 3D pore object is defined as the ratio between the smallest eigenvalue and the largest one for the

inertia eigenvectors, where inertia eigenvalues and eigenvectors are calculated from the inertia tensor (equivalent ellipsoid) of the 3D pore object. Therefore, the aspect ratio ranges between 0 and 1; a value of 1 corresponds to a sphere. The calculation of 3D aspect ratios was performed on Dragonfly. Both pore connectivity and connectivity density indicate the degree of connectivity in the pore network, but their definitions are different. Pore connectivity (expressed in %) is defined as the number of void voxels in the largest percolating pore object (cluster) divided by the total number of voxels attributed to pores in the VOI [46, 47]; it is a fraction of porosity, and equal to 100% when all the pores in the system are percolating. For uncracked samples, no percolating pore system is obtained for the whole image stack. In such an instance, pore connectivity is the measurement of the percolating pore object limited to the lower half-height of the sample. In comparison, the measurement of connectivity density required further computations with the BoneJ plugin [48-50] in Fiji. The pore object (network) was first skeletonized with a topology-preserving medial axis algorithm allowing branch (i.e., trabecule) and junction analysis [51]. Then, the number of connected trabecules in the VOI was measured, and the connectivity density (expressed in μm^{-3}) was defined as the number of trabecules divided by the VOI [49, 50]. The tortuosity was quantified by generating random walkers within the skeletonized pore network and recording their travelled free distance with the AnalyzeSkeleton [52] plugins in Fiji. The tortuosity is defined as the mean free distance divided by the Euclidian distance from the start point to end point [52-54]. In this paper, VOI refers to the whole sample volume since a global analysis was conducted.

3. Results and discussion

3.1 Material composition and characterization results

XRD analysis (Figure 8) for binder fragment displays the presence of calcite as the main crystalline phase; analcime, albite, augite, ettringite, leucite, quartz, and sanidine were detected as minor components. Furthermore, XRD shows a hump centered in the range 20° - 40° 2θ due to the glassy content of the pozzolan; it could be ascribed to amorphous calcium silicate and aluminate pozzolanic cementitious gels [55].

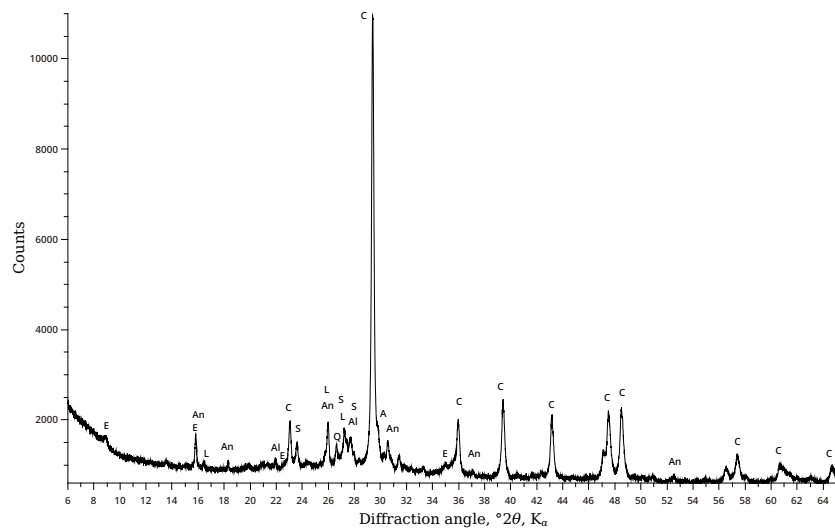


Figure 8. XRD spectrum for binder sample of pillar mortar: A=augite, An=Analcime, Al=albite
C=calcite, E=ettringite, L=leucite, Q=quartz, S=sanidine.

The following information can be obtained from the DT-TG results: a) reactions peak temperature and main effect (endothermic or exothermic); b) total weight loss of the sample, TWL (evaluated

in the temperature range 20°-900°C); c) physical bound water content, PBW (as weight loss in the 20°-120°C range); d) hydrated salts content, SC (as weight loss in the 120°-200°C range); structural bound (or hydraulic) water content, SBW (as weight loss in the 200°-600°C range); e) CO₂ amount deriving from calcination of CaCO₃ phases (as weight loss in the 600°-900°C range). The main endothermic peak in the DT curves (Fig. 9) is assigned to calcite decomposition (810°±21°C). Four smaller endothermic peaks were also observed with increasing temperature: the first one (165°±12°C) can be attributed to ettringite, the second and third (465°±15°C, and 540°±13°C) to thermal decomposition of calcium (alumino) silicate hydrate (C-(A-)S-H) products [56, 57] and calcium carboaluminate hydrate compounds [58], respectively; the fourth small peak (850°±6°C) is attributed to a carbonate phase.

C-(A-)S-H main peak is not detected inasmuch as it is overlapped by the ettringite one which, in fact, appears quite wide and shallow. The second small endothermal peak is also wide and shallow probably due to the thermal decomposition of analcime [59]. Moreover, TG curves show that an almost constant weight loss rate is measured in the temperature range 20°-600°C, [60] which is related to the decomposition of the above mentioned hydrated phases. All the weight losses of the three binder samples (S1, S2 and S3 corresponding to the cement paste of DP and WP), together with their “hydraulicity index” ($R = \text{CO}_2/\text{SWB}$), are reported in Table 2.

Table 2. DT-TG analysis of S1, S2, and S3 samples.

	PBW	SC	SBW	CO ₂	R	TWL
S1	1.15	1.68	5.93	13.84	2.33	22.60
S2	1.34	1.42	6.25	14.70	2.35	23.71
S3	1.43	1.40	6.17	14.18	2.30	23.18

The analysis was performed solely on the cement paste (without any calcareous sand aggregate) as with samples S1, S2, and S3. The amount of CO₂ release is a useful indication of the calcium hydroxide content in the original binder and, therefore, becomes one metric to discriminate typical lime mortars from hydraulic mortars [10, 61]. Based on this observation, the value of R inversely expresses the hydraulic character of a mortar: R values greater than 10 indicate lime mortars while, when R values are lower than 10, the mortar is defined hydraulic (called also “pozzolanic” when $R < 3$) [60]. R determinations indicate that all the investigated samples are pozzolanic. As an example, DT-TG thermogram of one of the three binder samples is reported in Figure 9.

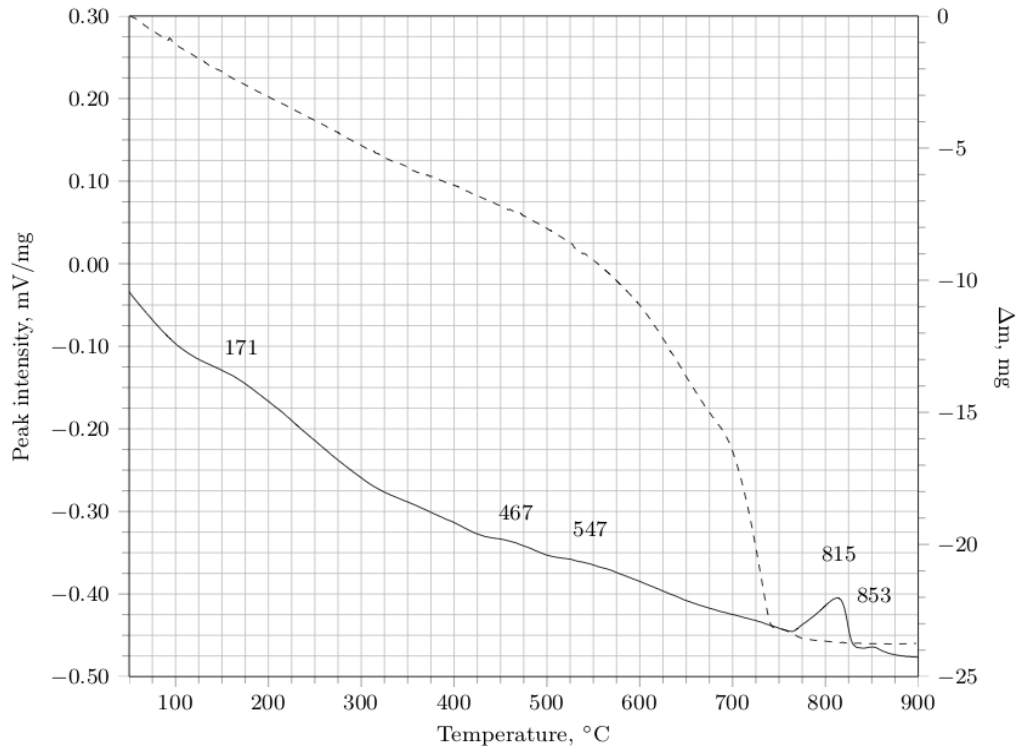


Figure 9. DT (solid line)-TG (dashed line) curves for binder sample of pillar binder (Δm is the mass variation with respect to the 100 mg initially present in the crucible).

SEM images for mortar fragments are reported in Figure 10. CaCO_3 particles are present either as prismatic crystals with a slightly etched surface morphology (Figure 10 (a)) or as tiny irregular aggregations (Figures 10 (a) and (b)). SEM images also revealed the presence of both calcium silicate hydrates and C-(A-)S-H shaped as honeycomb and needle-like shaped solids (Fig. 10 (c) and (d)) [62]. Finally, organic fragments were also detected (Fig. 10 (e) and (f)) [63].

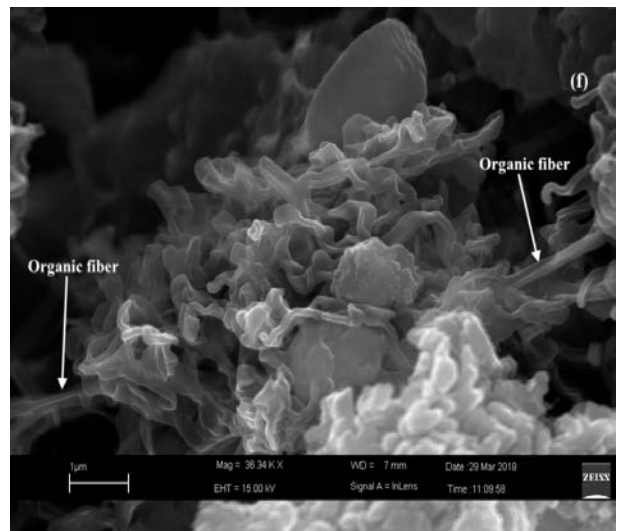
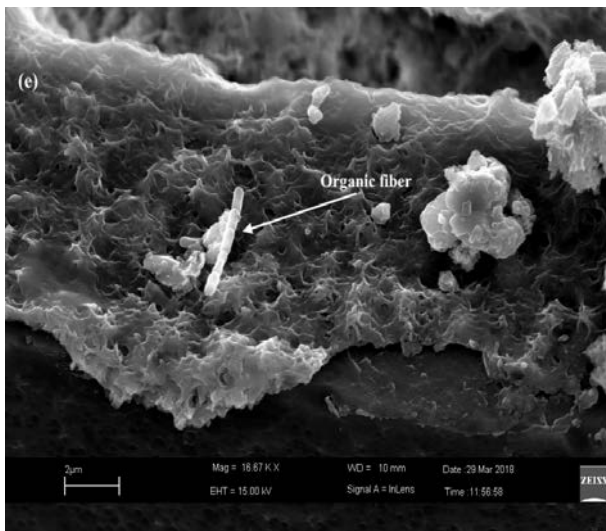
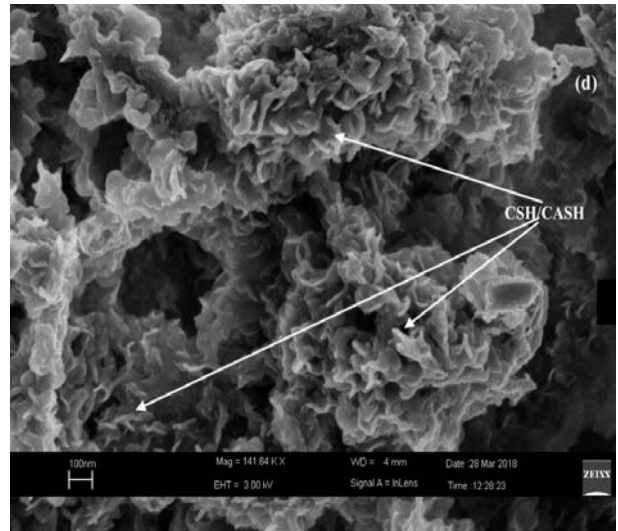
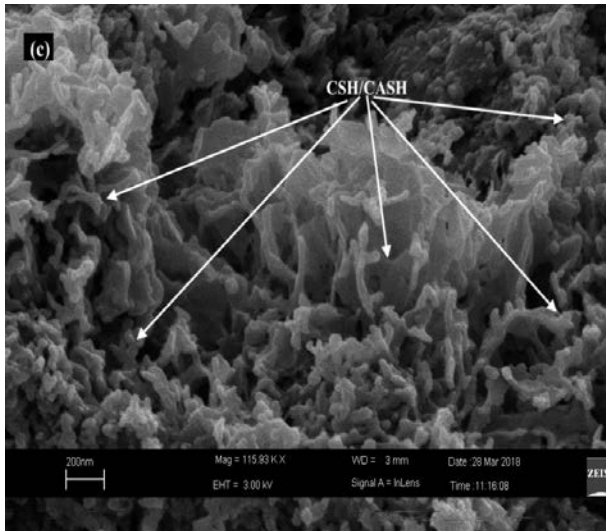
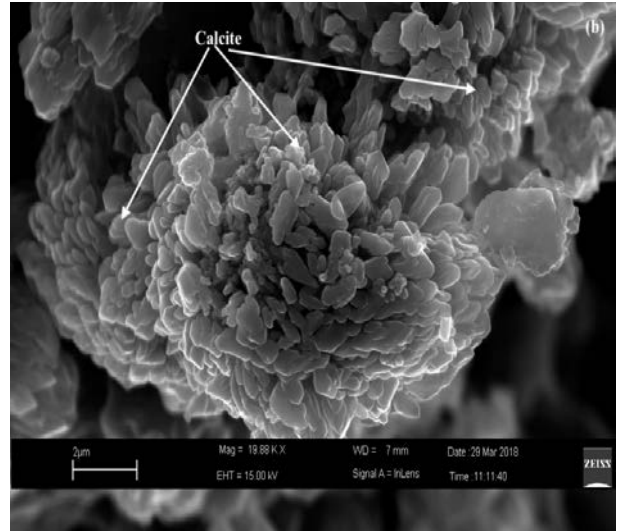
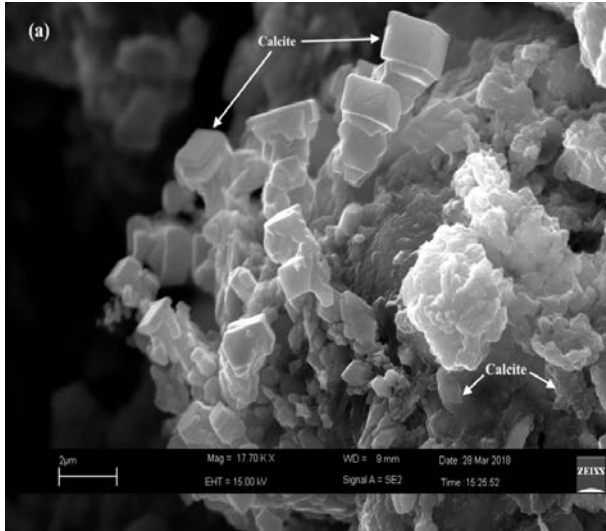


Figure 10. SEM images of mortar pillar fragments

The reproducibility of mercury porosimetry measurements among the three replicates was successful; in fact, the greatest total porosity value was 36.2% while the lowest was 34.5%, respectively corresponding to a total cumulative intruded Hg volume equal to 248.4 and 217.7 mm³/g. As an example, Figure 11 reports the cumulative (a) and derivative (b) Hg volume for one of the three inspected samples; it can be noted a quite sharp unimodal pore size distribution centered on a threshold pore radius equal to 0.79 μm (being a value related to the other two mortar fragments equal to 0.77 and 0.86 μm, respectively). According to MIP results from Herculaneum-Roman mortars [60], the examined samples belongs to the “medium degree of porosity (20-40%)” group. Besides, the measured pore sizes in these mortars are more than one order magnitude larger than the usual pore sizes of the percolating pore system of modern Portland cements (C-A-S-H pores). The latter are reputed in a 10-40 nm range [64-66]. Such small pores are present in non-negligible amounts in the PSD given in Figure 11, although they do not correspond to the peak size. The peak pore sizes of 0.77-0.86 μm may be attributed to paste damage due to Hg pressure, or to sample damage during its preparation for Hg porosimetry.

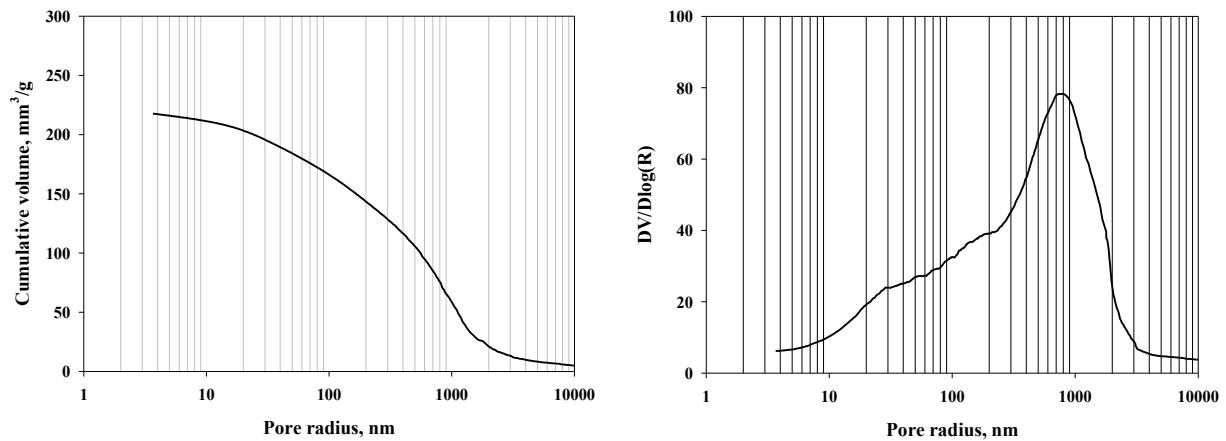


Figure 11. Cumulative (left) and derivative (right) Hg volume vs. pore radius for mortar pillar fragment.

3.2 Microtomography results

3.2.1 Microstructure analysis of dry Pompeii sample before and after introducing cracks

To visualize the 3D cracking patterns of the dry Pompeii (DP) sample once it was cracked by mechanical compression, 3D renderings of uncracked and cracked DP were reconstructed (Fig. 12 (a) and (b)). Note that there is no apparent difference between the left-hand side image and the right-hand side image. Direct 3D visualizations of the reconstructed sample do not present the global cracking pattern because the cracks are inside the DP and did not reach the outside surface. As shown in the XY plane cross-section slices at a height of 14mm (Fig. 12 (c) and (d)), the cracks propagated in the region $\{X, Y: 15 \text{ mm} \leq X \leq 25 \text{ mm}, 0 \text{ mm} \leq Y \leq 10 \text{ mm}\}$, that was not visible from the 3D renderings of reconstructed external surface. The direct 3D renderings of

reconstructed tomograms cannot visualize the complicated 3D cracking patterns in concrete, especially the internal cracks.

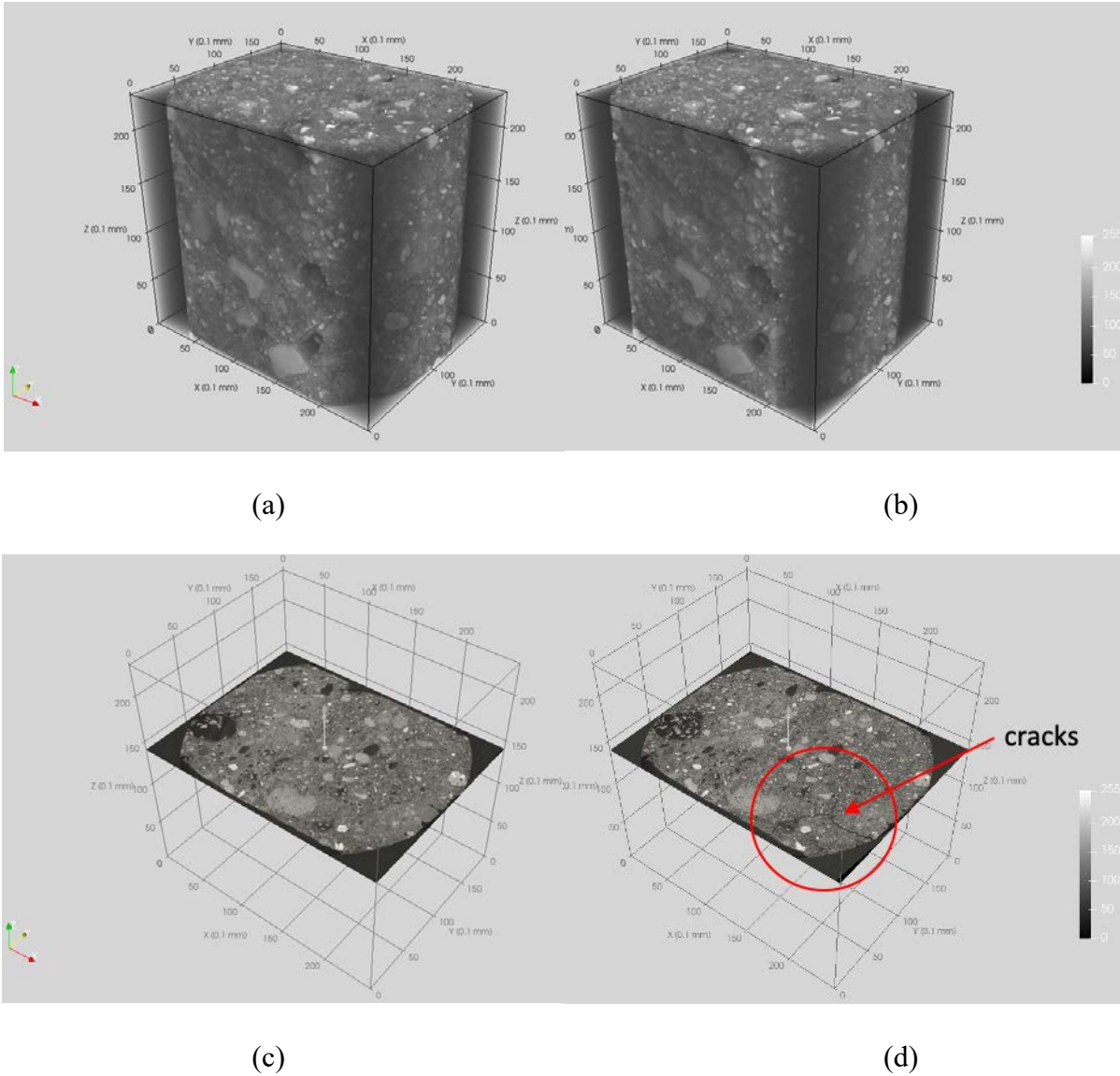
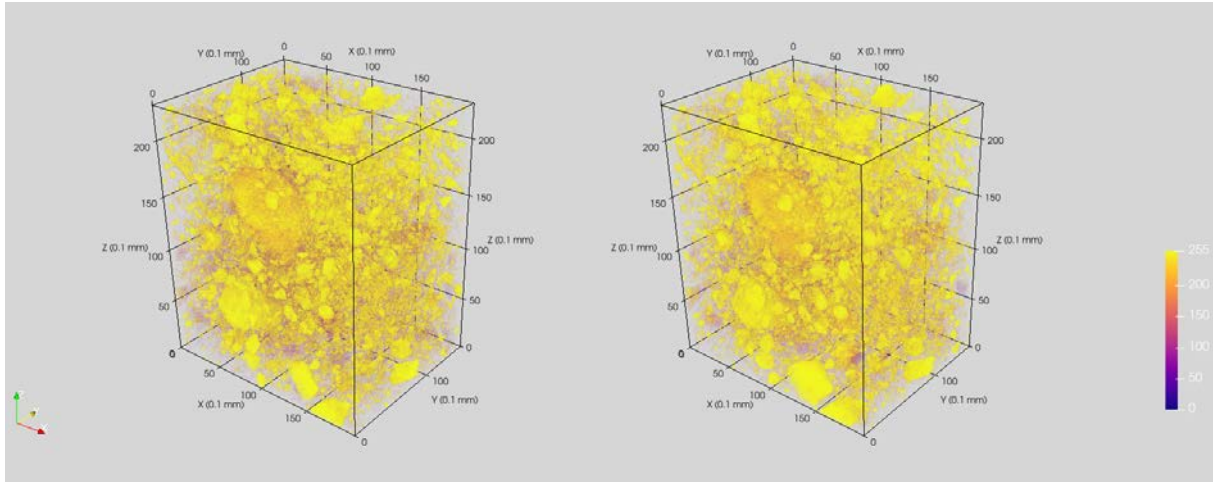


Figure 12. 3D rendering of reconstructed tomography for dry Pompeii sample: (a) uncracked DP, (b) cracked DP. And 3D rendering of 2D slice at specific height (14 mm) for dry Pompeii sample: (c) uncracked DP sample, (d) cracked DP sample.

The phases segmentation from reconstructed μ CT images offers accurate, complementary results for both qualitative understandings of complex 3D microstructure and quantitative evaluation of key material properties of the samples. As shown in Fig. 13, the aggregate phase and pore phase at both uncracked and cracked states were rendered to reveal the microstructure of DP. The segmentation results of region $\{X, Y, Z: 2.5 \text{ mm} \leq X \leq 22.5 \text{ mm}, 0.1 \text{ mm} \leq Y \leq 19.9 \text{ mm}, 0 \text{ mm} \leq Z \leq 25 \text{ mm}\}$ in the original coordinate system (Fig.11) were rendered respectively to avoid the misclassified background phase and stage phase. For the color bar, bright value shows a high probability that the voxel is classified as the indicated phase, while the dark color indicates that the voxel is not likely to be of the indicated phase. Comparing Fig. 13 (a) and (b), the distribution and particle sizes of aggregate phase are nearly the same before and after introducing cracks. The consistent segmentation results of the aggregate phase for the two μ CT dataset scanned separately verified the accuracy of applied segmentation algorithms.

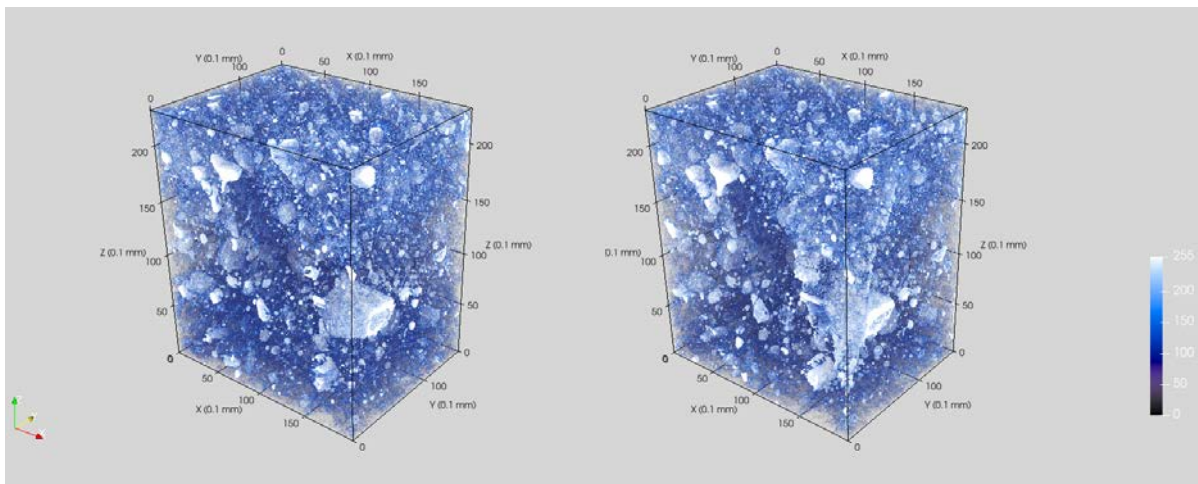
The segmented pore phases (Fig. 13 (c) and (d)) were rendered to reveal the difference between pore networks. Sample DP with varied pore sizes and evenly spatial distributions is shown in Fig. 13 (c) and (d). In the region $\{X, Y, Z: 12.5 \text{ mm} \leq X \leq 20 \text{ mm}, 0.1 \text{ mm} \leq Y \leq 10 \text{ mm}, 3 \text{ mm} \leq Z \leq 25 \text{ mm}\}$, new pore phases (white voxel) emerged due to the propagation of multiple cracks and formed a triangular fracture plane after the mechanical compression test. By comparing the cracked pore phase and aggregate phase, most cracks propagated along the edges of aggregates. This result suggests that the interface transition zones (ITZs) in the dry Pompeii sample were the weak zones where crack initiation and propagation occurred. Further segmentation could be done to visualize the introduced cracks without the initial pores, but it is very challenging to further

separate them due to the similarities of their grey level, particle size, spatial shape, and spatial distribution.



(a)

(b)



(c)

(d)

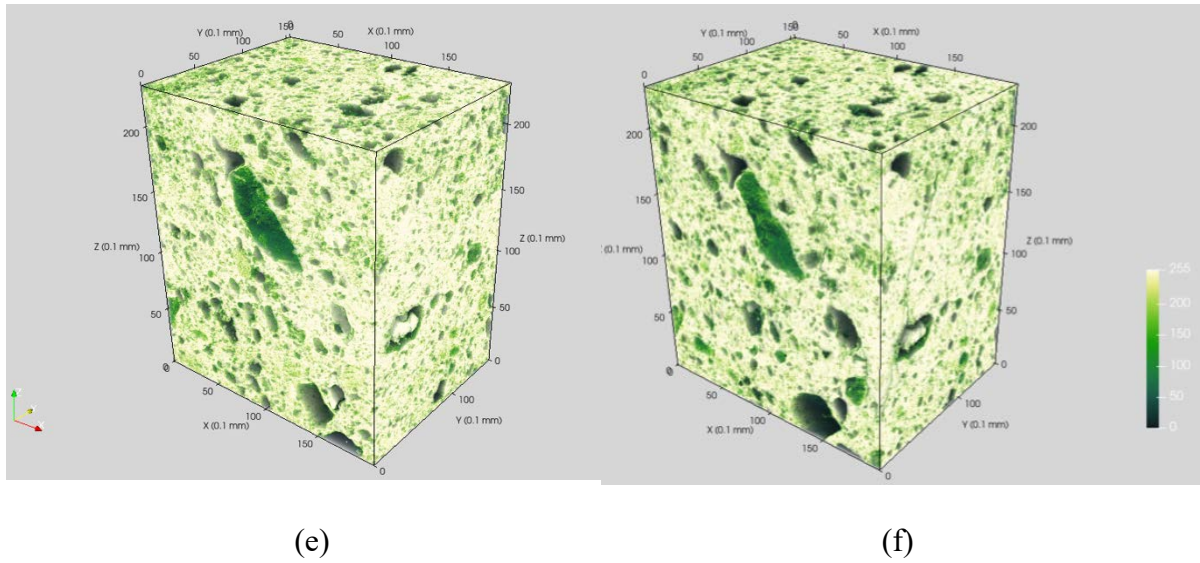


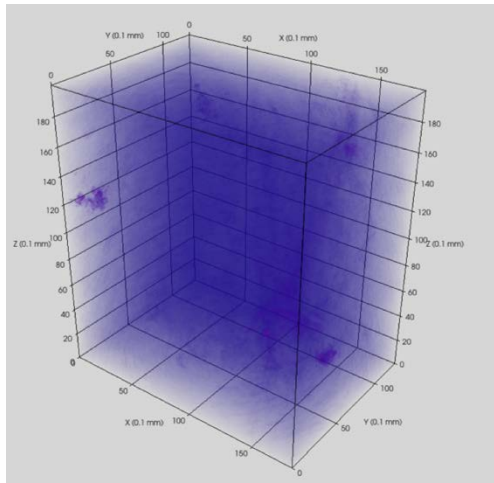
Figure 13. 3D rendering of segmentation results for DP: (a) aggregate phase of uncracked DP, (b) aggregate phase of cracked DP, (c) pore phase of cracked DP, (d) pore phase of cracked DP, (e) matrix phase of cracked DP, (f) matrix phase of cracked DP.

DVC analysis provides both qualitative understandings of complex 3D fracture patterns and quantitative evaluation of the damage. 3D displacement maps, major principal strain field, and residual error field (Fig. 14) were calculated using C8R DVC as described in the digital volume correlation section. For the color bar, the bright value indicates a high residual error, displacement, or strain. There are few residual errors, and the maximum error is under 0.1, which indicated a high accuracy of DVC calculation. In the displacement maps, a steep strain gradient indicates the presence of a crack. In the principal strain field, the maximum of principal strain is a measure of the crack opening displacement magnitude.

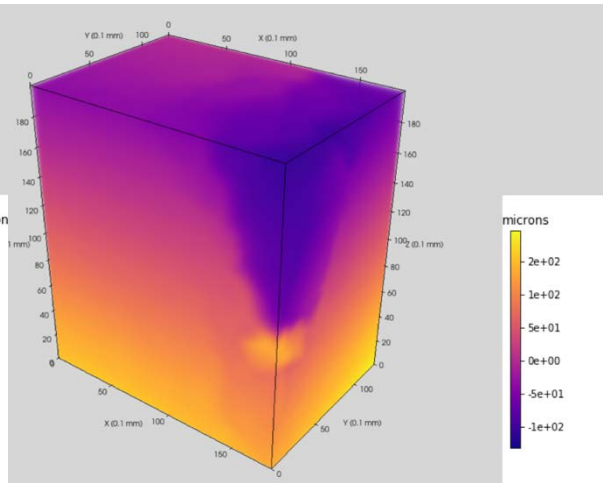
From the visualization of the 3D fracture pattern (Fig. 14), the dry Pompeii sample DP presents a ductile fracture pattern and consumes more energy than the brittle fracture pattern. In ordinary

Portland cement concrete, crack paths preferentially develop in the porous ITZ zone between the fine-grained cement paste and largely inert sand and gravel aggregate; cracks paths usually only have few microcracks and one macrocrack, and the sample presents a brittle fracture mechanism. However, the fracture behavior of DP, similar to the Type 5 failure of a typical cylindrical concrete during uniaxial compression (ASTM C39) [67], introduced extensive micro and macro cracks propagation. Type 5 fracture occurred due to the unbonded caps during the loading, and ultimate capacity of the specimen may have not been attained. The multiple micro/macro crack propagations and the wider dispersion of cracks caused a load redistribution. Additional energy was absorbed by the diffuse networks of micro and macro cracks than the standard Type 5 fracture with single localized macrocrack.

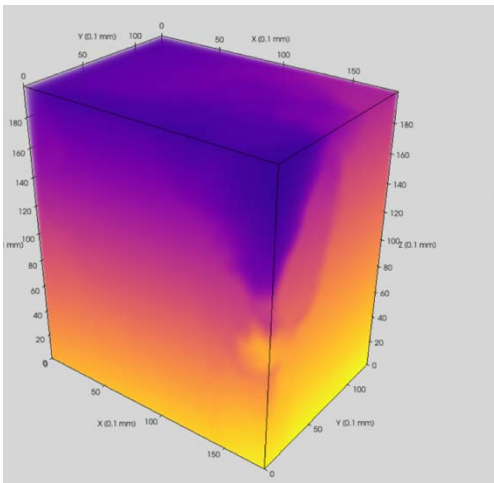
By comparing Fig. 14 (f) and Fig. 13 (d), 3D fracture pattern from DVC analysis and newly emerged pore phases provided similar results of crack paths. The macro crack propagations appeared in the top corner region $\{X, Y, Z: 12.5 \text{ mm} \leq X \leq 20 \text{ mm}, 0.1 \text{ mm} \leq Y \leq 10 \text{ mm}, 3 \text{ mm} \leq Z \leq 25 \text{ mm}\}$ of DP. The morphology of macro cracking networks formed a triangular fracture plane. Besides, the calculated normal directions of the fracture plane from the two methods were the same. The above results verified the accuracy of both image segmentation and DVC analysis.



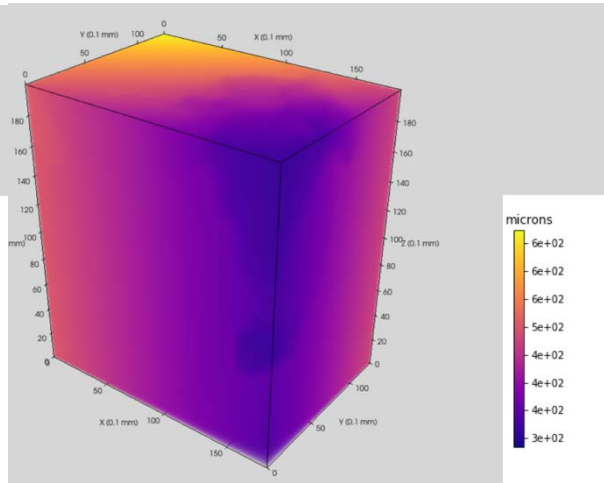
(a) Residual Error



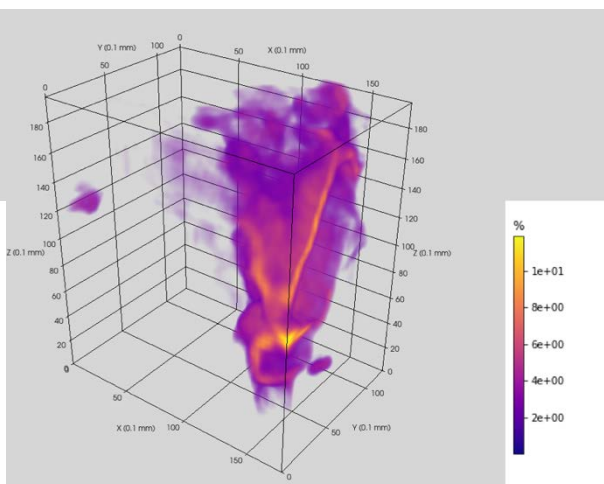
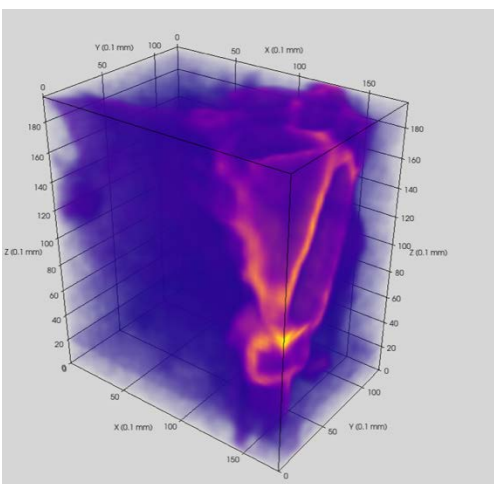
(b) Displacement Ux



(c) Displacement Uy



(d) Displacement Uz



(e) Major principal strain ϵ_{eq} (f) Visualization of Cracking

Figure 14. 3D renderings of major residual error field, displacement fields (U_x , U_y , U_z), principal strain ϵ_{eq} and cracking propagation in DP

3.2.2 Microstructure analysis of wet Pompeii sample before and after introducing cracks

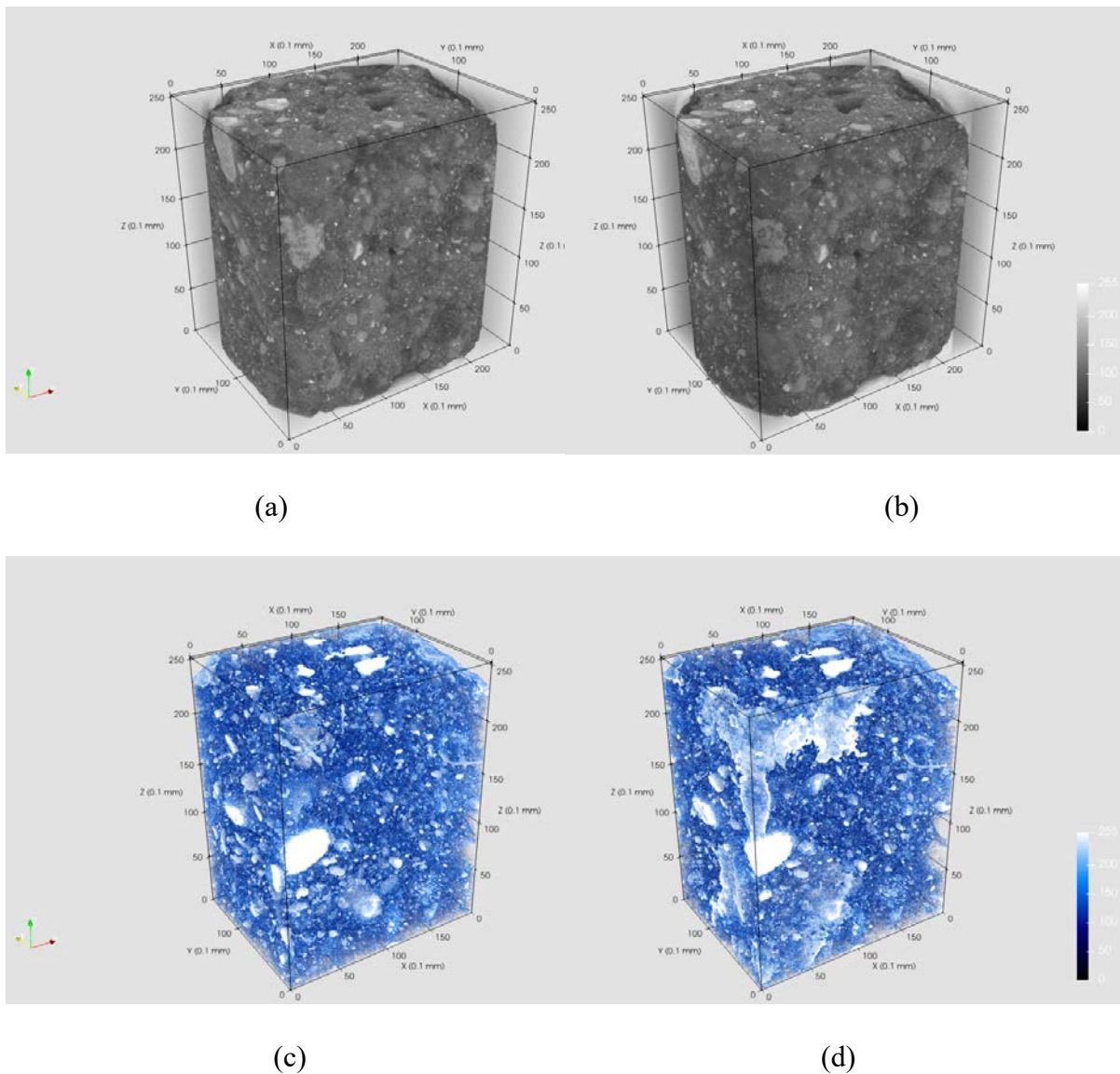
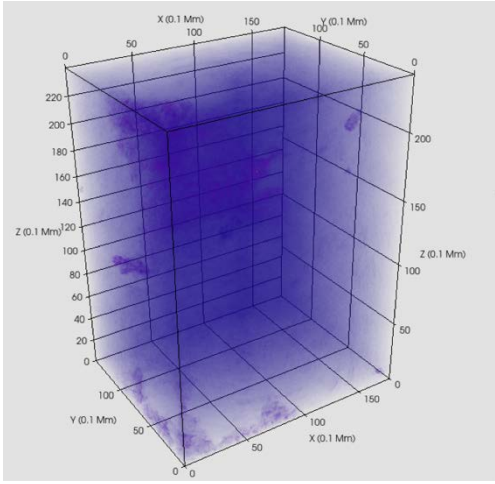


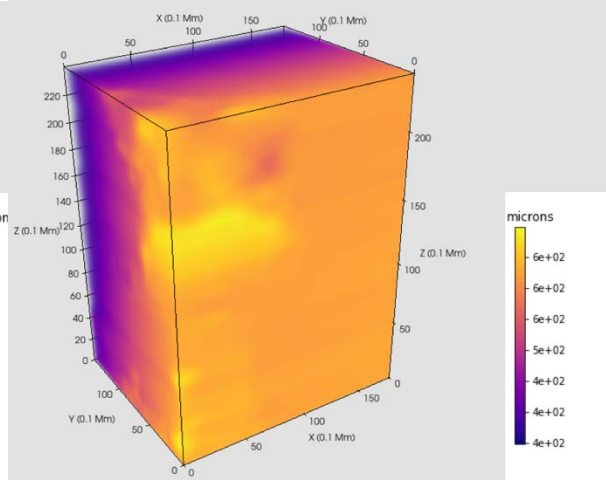
Figure 15. 3D rendering of reconstructed tomography and segmentation results for WP sample

(a) uncracked WP sample, (b) cracked WP sample, (c) pore phase of uncracked WP sample, (d) pore phase of cracked WP sample.

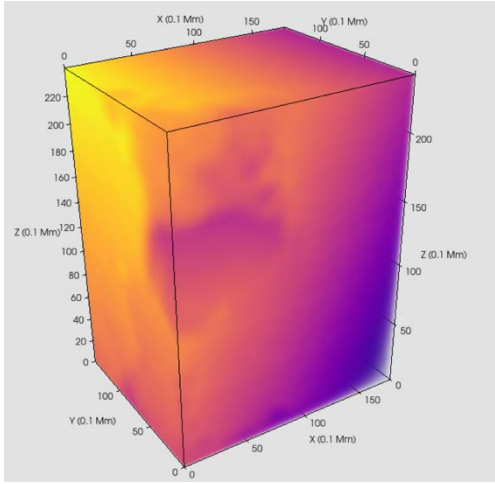
The same segmentation and visualization procedures were applied on the WP dataset. The pore phase at both uncracked and cracked states (Fig.15) was rendered to reveal the microstructure of the WP sample. Similar to the DP sample dataset, the segmentation results of region $\{X, Y, Z: 2.5 \text{ mm} \leq X \leq 22.5 \text{ mm}, 0.1 \text{ mm} \leq Y \leq 19.9 \text{ mm}, 0 \text{ mm} \leq Z \leq 25 \text{ mm}\}$ in the original coordinate system (Fig.15 a, b) were rendered respectively to avoid the misclassified background phase and stage phase. The WP sample also preserved the same aggregate size distribution after introducing cracks. There is no obvious deformation or relative displacement of aggregate particles, which is the same as the DP sample. When comparing the pore phase in uncracked WP sample and cracked WP sample, new pore phases (white voxel) emerged in the region $\{X, Y, Z: 0 \text{ mm} \leq X \leq 10 \text{ mm}, 0 \text{ mm} \leq Y \leq 10 \text{ mm}, 0 \text{ mm} \leq Z \leq 25 \text{ mm}\}$ where multiple cracks propagated. The cracking pattern of the WP sample is similar to the DP sample, but with wider macro crack propagation, cracks formed a large connected porosity network. In general, wet Pompeii sample and dry Pompeii sample have similar fracture patterns. Following results from DVC and 3D morphology analysis statistics will provide more evidence.



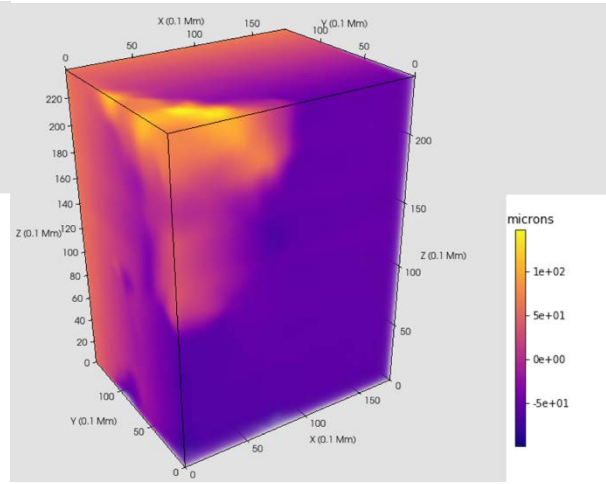
(a) Residual Error



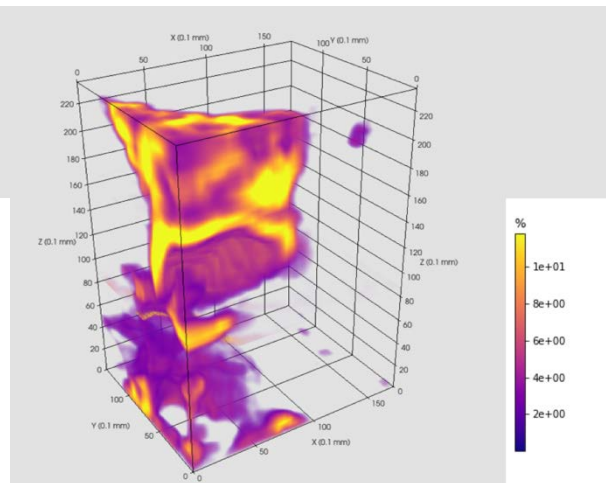
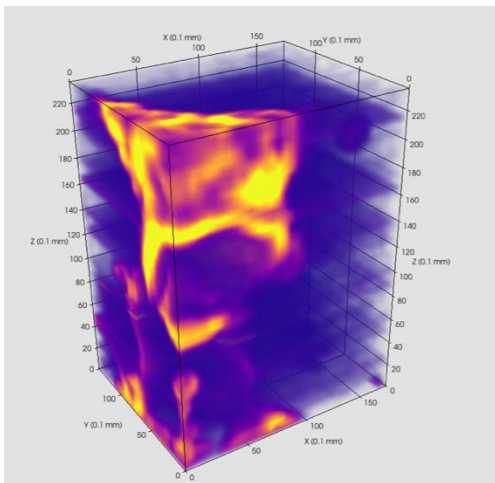
(b) Displacement Ux



(c) Displacement Uy



(d) Displacement Uz



(e) Major principal strain ε_{eq} (f) Visualization of Cracking

Figure 16. 3D renderings of major residual error field, displacement fields (U_x , U_y , U_z), principal strain ε_{eq} and cracking propagation in WP sample

As discussed in the previous section, DVC analysis was also performed on the WP sample using a regularized cubic 8 model with an element size of 20 voxels. The residual error in Fig.16 is low, indicating a low artifact and a high calculation accuracy for the displacement field and strain field. From the visualization of the displacement field, the whole WP sample nearly separates into three parts after the crack formation. By comparing Fig. 16 (f) and Fig. 15 (f), 3D fracture pattern from DVC analysis, and newly emerged pore phases gave similar results about crack paths. The macro crack propagations happened in the side corner region $\{X, Y, Z: 0 \text{ mm} \leq X \leq 10 \text{ mm}, 0 \text{ mm} \leq Y \leq 10 \text{ mm}, 0 \text{ mm} \leq Z \leq 24 \text{ mm}\}$ of WP sample, which corresponds to the porosity distribution in Fig. 15 (f). The above results again verified the accuracy of image segmentation. The multiple micro and macro cracks propagations and broader dispersion of cracks in the WP sample are similar to the ductile cracking propagation and fracture pattern in the DP sample. Therefore, the wet Pompeii sample, although suffering from long-term water erosion, still has load-bearing capacity and durability. Our previous paper extensively discussed how needle-like and fiber-like phases contribute the mechanical resistance and durability [1, 3, 6].

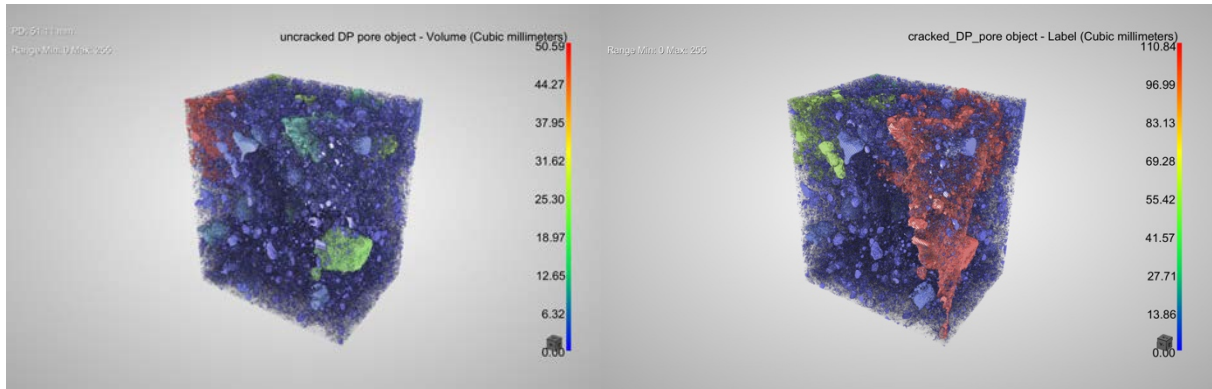
3.2.3 3D statistical analysis

A more detailed cracking pattern analysis is conducted through 3D connectivity calculations for the pores and cracks. The segmented images of the pore phase were imported as ROIs files into Dragonfly. Object analysis statistics were performed to calculate the volume, volume diameter, porosity, and pore (network) connectivity, as shown in Table 3. Note that the porosity of uncracked samples from μ CT is much lower than the porosity obtained by MIP on the uncracked mortar fragments, because μ CT only characterized a fraction of total porosity measured by MIP. There is no percolating pore network in the whole volume of the uncracked samples obtained, owing to μ CT alone; a percolating pore system is obtained only for the lower sample half height. This means that the fully percolating pore network in uncracked Pompeii samples is below the resolution of μ CT (below $9.5 \times 2 = 19 \mu\text{m}$), and hence, fluid permeability is due to pores smaller than this value; with a typical 1D Katz-Thompson model for fluid permeability (with a porosity of 8.68 or 13.48%, a critical pore size of $19 \mu\text{m}$, a tortuosity of 1) [68], this means that permeability is smaller than $1-2 \times 10^{-13} \text{ m}^2$. The comparison of pore structures between ancient Pompeii concrete and modern Portland cement paste/concrete is discussed in section 3.4. After introducing cracks, both DP and WP samples only have a minor increase ($< 0.5 \%$) in porosity and a minor decrease of tortuosity, but a significant increase ($\sim 10\%$) in pore connectivity. Because of the low pore connectivity without the largest pore cluster in cracked samples, this result suggests that the volume of the introduced cracks is small. Note that percolating pore networks are only observed after introducing cracks, suggesting that the detected percolating pore networks in the cracked samples are composed both of initial large pores but most importantly of introduced cracks.

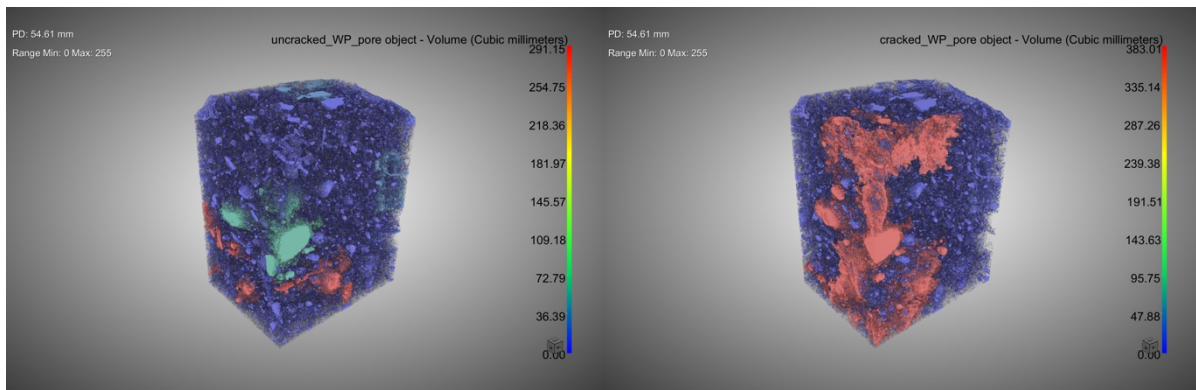
Table 3. Porosity and pore connectivity of sample DP and WP before and after cracking, as given by μ CT.

Concrete	Total porosity	Connectivity	Connectivity density (um ⁻³)	Tortuosity (Mean ± Standard deviation)
uncracked DP	8.68%	0% (9.37% at half height)	2.30E-09	1.32 ± 0.43
cracked DP	9.04%	21.22%	3.73E-08	1.30 ± 0.41
uncracked WP	13.48%	0% (26.74% at half height)	8.50E-09	1.26 ± 0.37
cracked WP	13.68%	39.40%	9.05E-08	1.25 ± 0.38

Figure 17 visualizes the 3D pore connectivity of both DP and WP and shows similar cracking patterns. Only one major macro crack is observed at the side corners of the DP sample by comparing (b) and (a). Multiple pores ranging from 0 to 30 mm³ (i.e., 0 to 1.9 mm if pores are assumed perfectly spherical) within this area are connected by this macro crack, which significantly increases the connectivity of pores (from 9.37% to 21.22% for DP) and water penetration rate within this area. However, the majority of large pore objects outside this area preserve their volume, and the connectivity is weak, because the pore connectivity without the largest pore for cracked DP sample is very low (only 13.3% of total porosity). This result means that the water penetration rate outside the fracture zone would not vary significantly when the cracks are introduced. Similar results can be observed for the WP sample when comparing (d) and (c). The difference between DP and WP is that the major macro crack of WP has a larger volume and connects more pores than that in the DP. Therefore, the water penetration in cracked WP should be faster than in the cracked DP. Fig.23 and 28 in section 3.3 attest to the deductions related to the water penetration experiments.



(a) (b)



(c) (d)

Figure 17. 3D rendering of connected objects for pore phase in the order of volume:

(a) uncracked DP sample, (b) cracked DP sample, (c) uncracked WP sample, (d) cracked WP sample.

The discrete pore size histograms in DP and WP for both uncracked and cracked states are statistically shown in Fig. 18, where the number of pore objects in the samples in different size ranges is plotted against the volume diameter. For both DP and WP, the cumulative number of pores with a diameter range of 100 μm - 3 mm decreased when the cracks were introduced. In the diameter range 4 – 10 mm, the cracked samples contain more pores than the uncracked samples. The largest pores (diameter > 4 mm) original in uncracked samples disappeared as individual

objects and were replaced by much larger pores (diameter > 6 mm). Considering the visualization results in Fig. 17 and Table 3, this result suggests that the major macro crack is likely to originate mainly from the largest pores and these cracks connect originally disconnected pores.

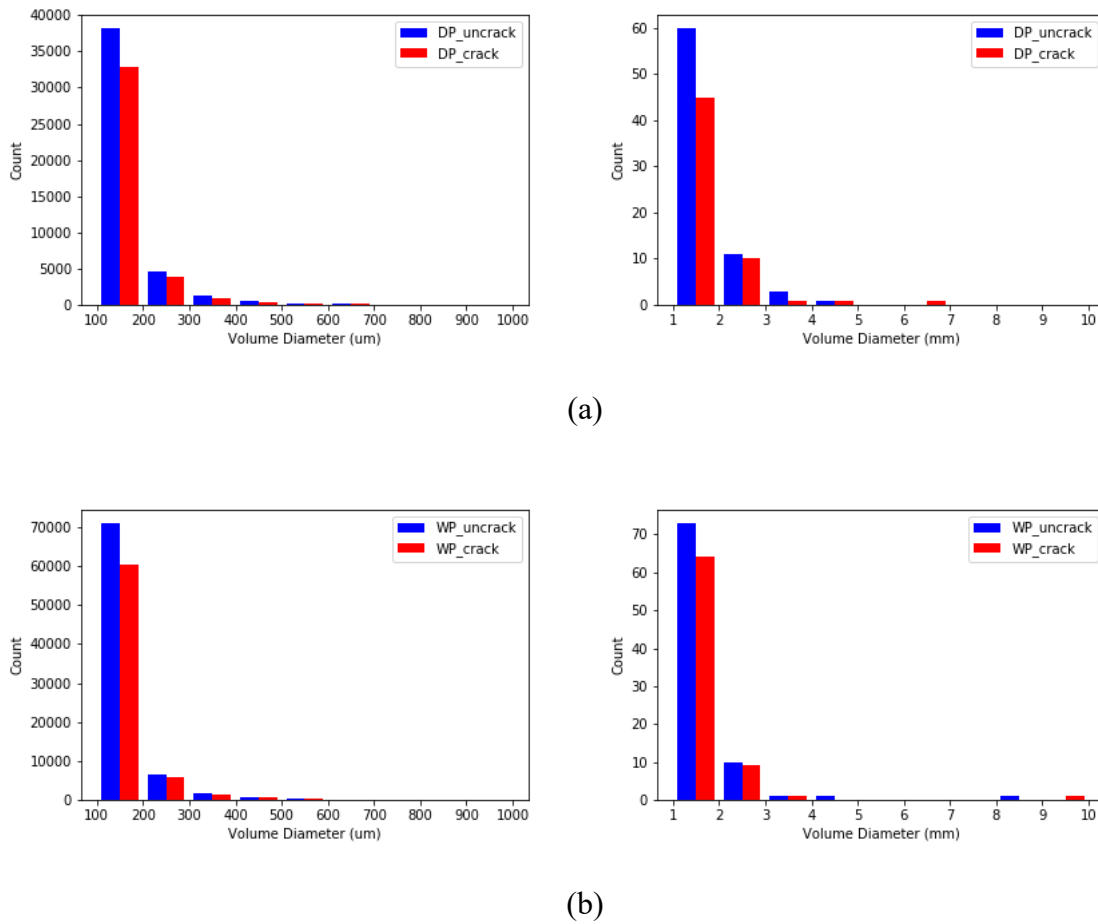
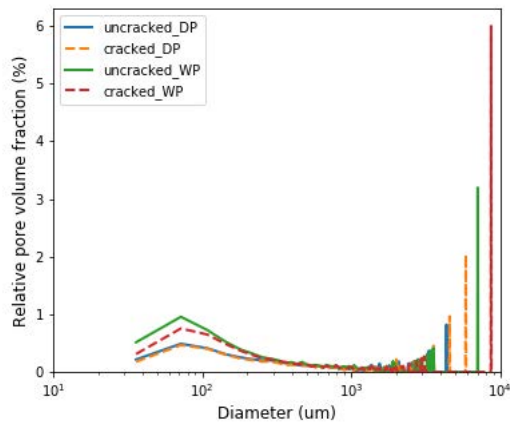
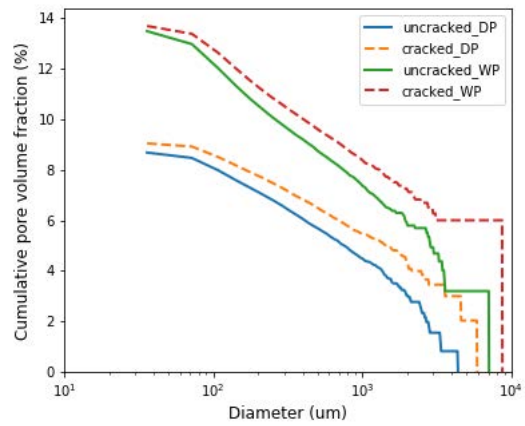


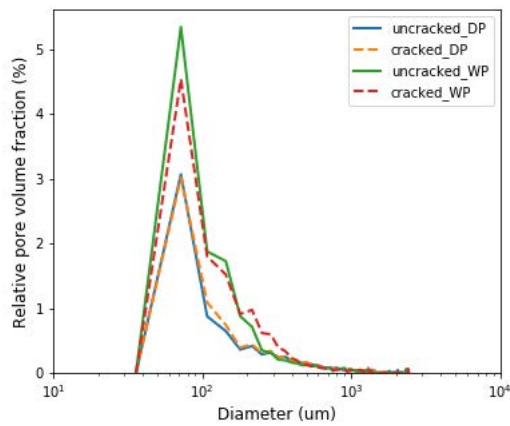
Figure 18. Discrete pore size histogram: (a) DP sample, (b) WP sample. For the left plots, the range of diameter is from 100 μm to 1000 μm . For the right plots, the range of diameter is from 1 mm to 1000 mm. The left plots characterize the small pores while the right plots characterize the large pores.



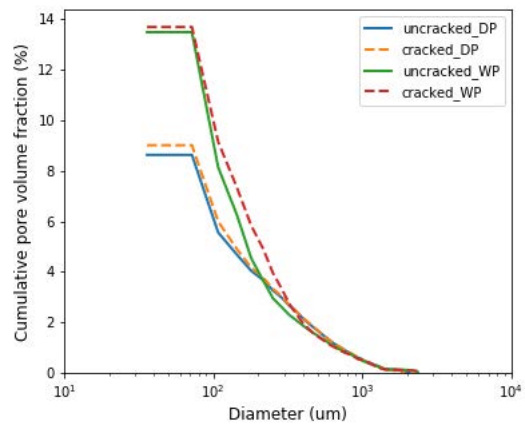
(a)



(b)



(c)



(d)

Figure 19. Combination of pore size distribution (PSD) of 3D segmented pore volumes, as obtained by (a) 3D relative Discrete PSD, (b) 3D cumulative Discrete PSD, (c) 3D relative Continuous PSD, (d) 3D cumulative Continuous PSD.

3D PSDs were computed by DPSD (Fig.19 a and b) and CPSD (Fig.19 c and d) methods. The 3D PSD is sensitive to the measurement method [43]. For both DP and WP, 3D DPSD provides a broad distribution of pore diameters from 36 μm to 8712 μm . The distribution increases

significantly for diameters larger than 3000 μm , and these large pore objects describe a large cumulative pore volume fraction. The comparison between the dashed curves (the cracked sample) and solid curves (the uncracked sample) shows that the pore volume fractions for diameter larger than 3000 μm increased significantly after introducing cracks. In comparison, the pore volume fractions for diameters smaller than 300 μm decreased, which is similar to the results from Fig. 17 and Fig. 18. However, with the DPSD method, any pore volume is represented by a single sphere even if the pore volume is composed of multiple connected pores and throats. Therefore, the DPSD is not a reliable method to provide PSD and usually exaggerates the diameter of pore volume, especially large connected pore volume, yet it provides useful information on pore volume repartition in a first approach.

The 3D CPSD accounts for the ability of a fluid to access a complex pore shape of a given size and also avoids the “ink bottle effect” as with MIP [69, 70]. For both Pompeii samples with complex elongated pores, 3D CPSD gives a more reliable PSD and peak pore size. From Fig 19 c and d, 3D CPSD provides a small distribution of pore diameters from 36 μm to 2400 μm , with a peak diameter at 50 -100 μm . The distribution decreases for diameters larger than 100 μm . Comparing the CPSDs of cracked samples and uncracked samples, the pore volume fractions of pore diameters from 100 μm to 170 μm slightly increased after introducing cracks into the DP. For WP, the increments in pore volume fractions after cracking occurred at a pore diameter from 170 μm to 400 μm . Note that the diameter corresponding to the increment essentially indicates the width of the introduced crack in the cracked DP and WP since the pore size in CPSD is quantified by Euclidian distance to between the nearest boundary. Therefore, the widths of introduced cracks in ancient Pompeii samples are mainly ranging from around 100 μm to 400 μm .

When comparing the total number of pores, porosity, and pore size distribution in the uncracked WP and uncracked DP, it is interesting to note that the uncracked WP has a larger porosity and greater number of pores within any range from 100 μm to 3 mm. Moreover, the introduced cracks in the WP are wider than in the DP. The difference may be attributed to the variability from one sample to the other and/or to small cracks induced by capillary effects during the air-drying of DP sample.

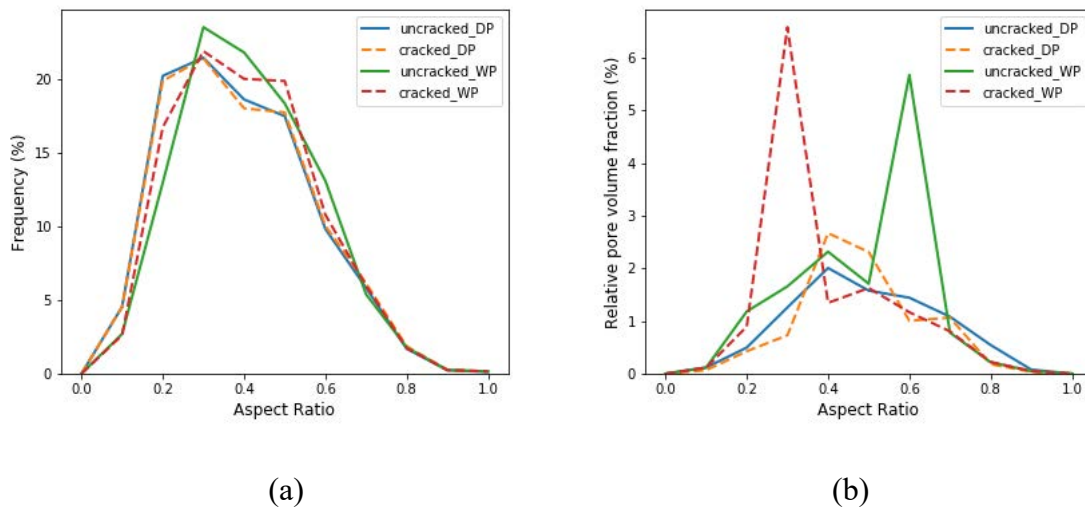


Figure 20. Distributions of 3D aspect ratio (elongation): (a) aspect ratio versus frequency; (b) aspect ratio versus relative pore volume fraction.

Fig. 20 shows the aspect ratio distributions, which statistically describe the shape of pores in different samples when they are modeled as ellipses. From Fig. 20 (a), the peak aspect ratio for both DP and WP samples ranges from 0.2 to 0.4, which corresponds to rather elongated pores (the smallest ellipse eigenvalue is 0.2 to 0.4 smaller than the largest one). The difference between the

curves of uncracked and cracked samples is small, suggesting that the introduced cracks only affect the shape of a very small number of pores. However, Fig. 20 (b) shows that this small amount of pores takes the majority of the volume fraction. For sample WP, the peak aspect ratio corresponding to the pore objects of ~6% volume fraction (~46% of total porosity) decreased from 0.6 to 0.3 after introducing cracks. Similar results are obtained for DP. After introducing cracks, the volume fraction of elongated pores with a peak aspect ratio of 0.4 increased from ~2% (23% of total porosity) to ~3% (35% of total porosity). The volume fractions of pores with aspect ratios close to 1 decreased after introducing cracks into both DP and WP. The above results indicate that the pores get connected by the introduced cracks and merged into more elongated pore networks considering the small variant of porosity.

3.3 Neutron radiography results

3.3.1 Water distribution in the originally wet Pompeii sample

Sample WP was maintained wet since its extraction from the structure. The white spectrum neutron transmission image in Fig. 21 (b) shows the water distribution in the uncracked WP sample. Water is evenly distributed in the whole WP sample, except for minor bright regions (see Fig. 25 (b)).

The neutron image (Fig. 21 (b)) is similar to the porosity density image (Fig. 22 (c)). The bright regions locate in zones with high porosity density (>0.5). The results indicate that the original wet Pompeii sample may have dried out sometime between the time of sample extraction and the

neutron radiography experiment as it was not sealed in a leak-free container. Indeed, water in the large pores exposed to the air is bound to evaporate first.

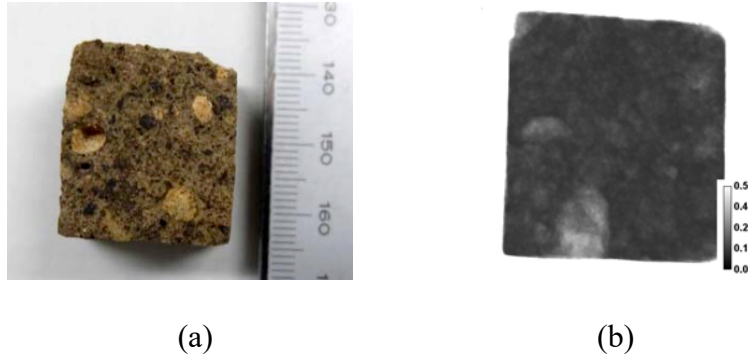
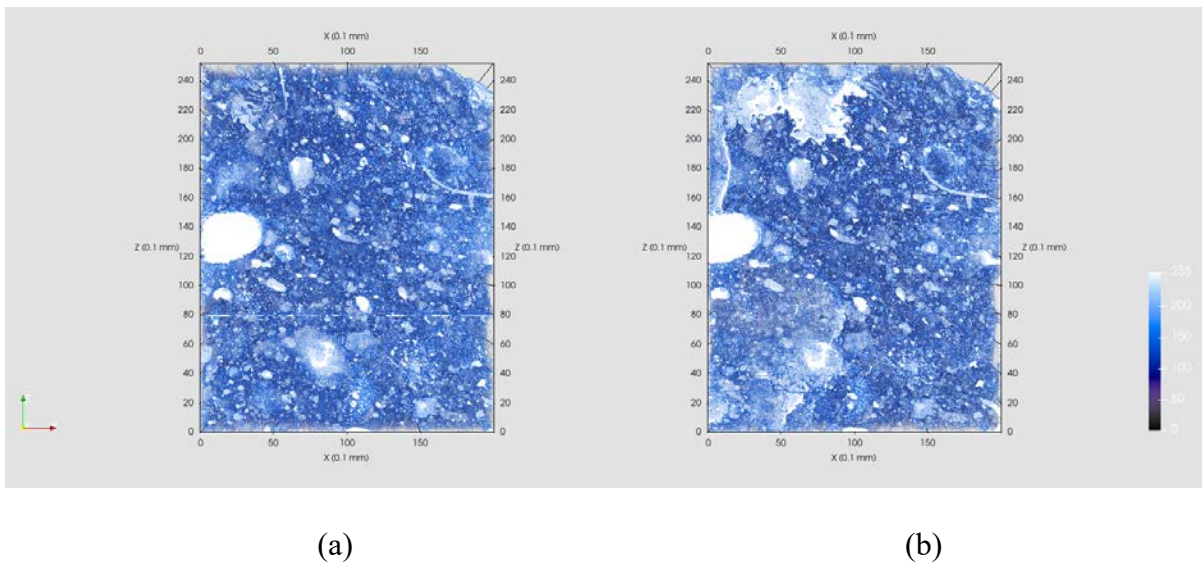


Figure 21. Photograph of uncracked sample WP (a) and white spectrum neutron transmission image (b) of uncracked WP measured in its original wet conditions (the sample was not dried intentionally after the extraction from the location site). The contrast in that image is due to attenuation by both concrete and water.



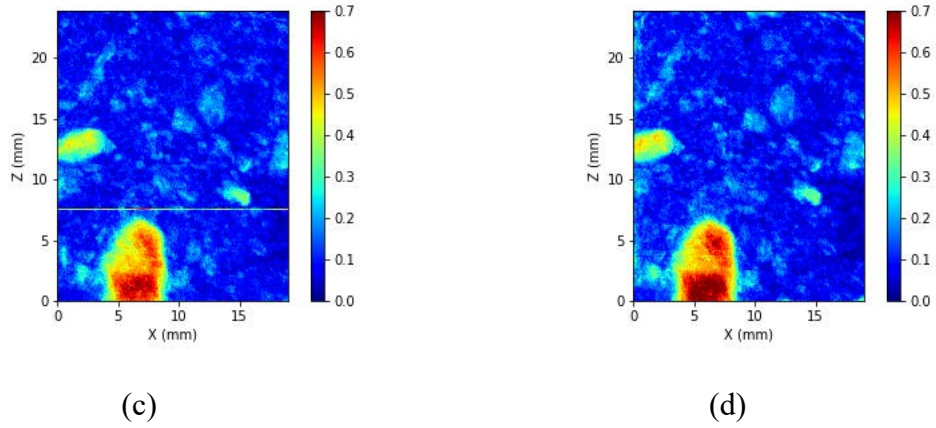


Figure 22. 2D view (XZ plane) of segmented pore phase for (a) uncracked WP sample and (b) cracked WP sample. 2D porosity projection (XZ plane) of (c) porosity density in uncracked WP sample and (d) porosity density in cracked WP sample. Plots (c) and (d) are projected from plots (a) and (b) along Y-axis. The porosity density value at each pixel is defined as the number of pore voxels divided by the total number of voxels along the Y-axis during the projection.

3.3.2 Quantitative map of water distribution

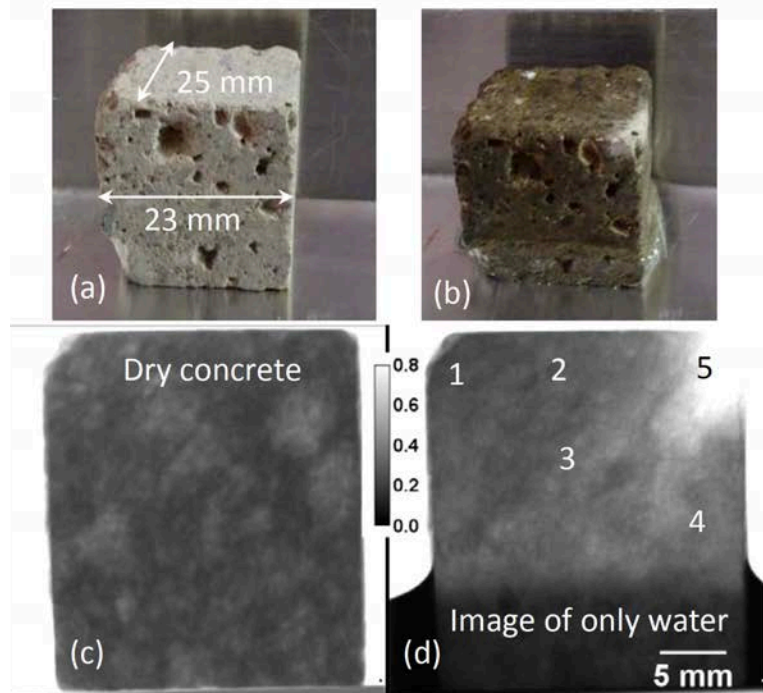


Figure 23. An example of step-by-step neutron radiography data analysis: (a) Photograph of the cracked dry concrete sample from Pompeii used in the experiment, (b) The same sample after absorption of water by capillary action (sample was partially immersed in water at the bottom), (c) White beam neutron transmission of the dry sample, (d) Neutron transmission image of water only (wet image was normalized by the image of the dry sample). The grayscale bar in (c), (d) indicates measured transmission values. The numbers in the image (d) indicate the areas of $2 \times 2 \text{ mm}^2$ for which the measured transmission is shown in Fig. 24.

An example of step-by-step neutron transmission spectra analysis and quantitative map of water distribution is shown in this section in the case of cracked DP sample. The same sample has been imaged using μ CT. Fig. 23 shows the photograph of cracked DP and its transmission image, obtained with a dried sample (left column) or with a fully wetted sample (right column); the contrast in neutron images (c) and (d) is provided only by water attenuation. After imaging the dry

sample for 16 minutes in the beam, water was added to the base aluminum container. Water was absorbed by the sample due to capillary forces over a ~20-minute period, during which white-spectrum transmission images were acquired in order to study the dynamics of water penetration. Following that, a set of energy-resolved images of the sample fully saturated by water were subsequently acquired with ~16 minutes integration.

Figure 23.d shows the neutron transmission image of water within the concrete sample, integrated overall energies. In this image, the contribution of concrete is removed by normalization of the wet image by the image obtained with the same sample in a dry state, taken at the beginning of the experiment (Fig. 23.c). Transmission spectra of the five regions marked in Fig. 23.d are shown in Fig. 24, together with the fitted theoretical transmission based on tabulated cross-sections [71]. The result of this analysis is a water distribution map within the concrete sample, shown in the image of Fig. 25.a, where different colors depict the amount of water integrated through the entire sample thickness. The bottom part of the sample was immersed in water and had no meaning in this reconstruction (white area of the image). The upper right corner did not fully saturate over the 20-minute experiment duration and has the smallest amount of water. The non-uniformity of water absorption in this particular sample was due to the presence of a diagonal crack, which was intentionally produced by the applied compressive stress load before the neutron imaging experiment.

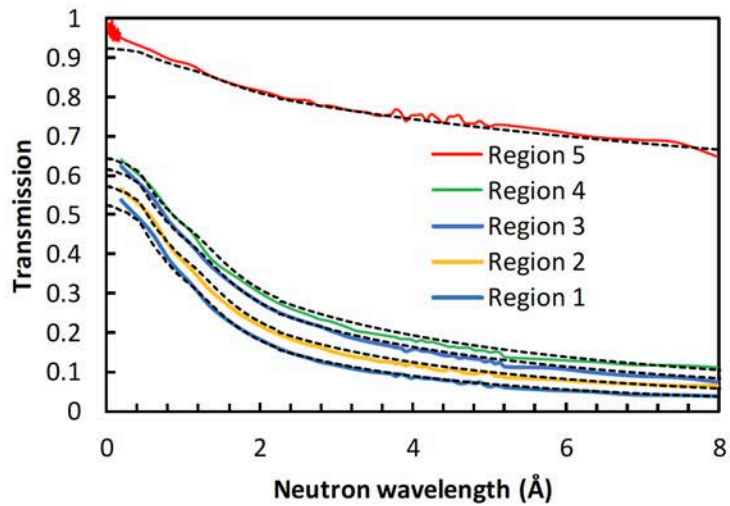


Figure 24. Measured (solid lines) and fitted (dash lines) neutron transmission spectra within the five regions of wet Pompeii concrete sample indicated by the numbers in Fig. 23.

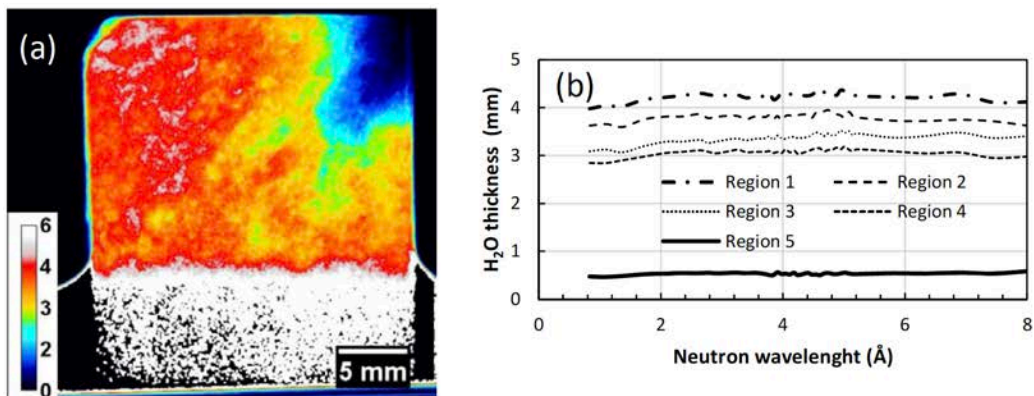
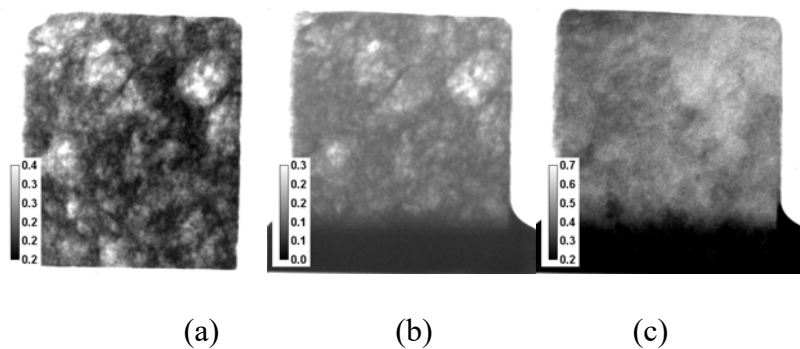


Figure 25. (a) Map of effective water thickness in the dry Pompeii concrete sample is reconstructed from the measured neutron transmission spectra. The color bar indicates the water thickness in mm. No data is reconstructed for the bottom part of the sample, which was immersed in water. The right top corner has not been saturated with water over the 20-minute tests. (b) Water thickness reconstructed from transmission measured at different wavelengths for the five areas of $2 \times 2 \text{ mm}^2$ shown by the numbers in Fig. 23.

The range of neutron energies which can be used for water quantification is checked by analyzing narrow-wavelength spectra individually (instead of fitting the entire transmission spectrum). Such analysis, in most cases, cannot be conducted for each individual pixel, as neutron statistics per pixel per narrow wavelength range is rather limited. However, to check the linearity of water quantification, pixels are grouped within a given region, as it was done over $\sim 2 \times 2 \text{ mm}^2$ areas for the results shown in Fig. 25.b. The reconstructed water thickness has a reasonably linear dependence on the neutron wavelength, although some reduction of water thickness is observed for both short (1-2 Å) and long (7-8 Å) wavelength ranges. These two ends of the neutron spectrum are most sensitive to the accuracy of background calibration, as neutron flux at these wavelengths was the smallest at the MLF facility in J-PARC. A more accurate background and scatter calibration can improve the linearity of these curves and thus improve the accuracy of the reconstructed water thickness.

3.3.3 Dynamics of water absorption in dry Pompeii sample before and after introducing cracks



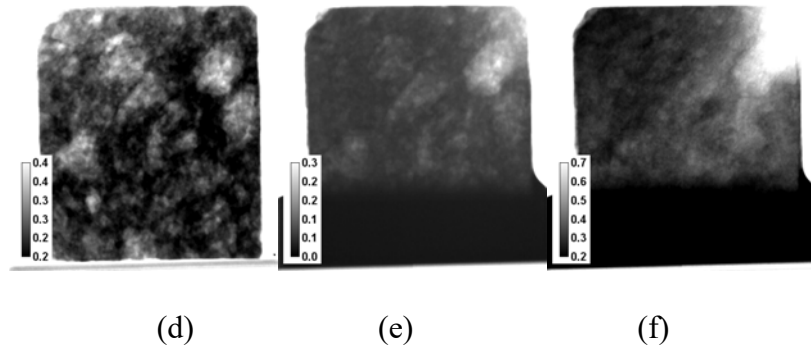
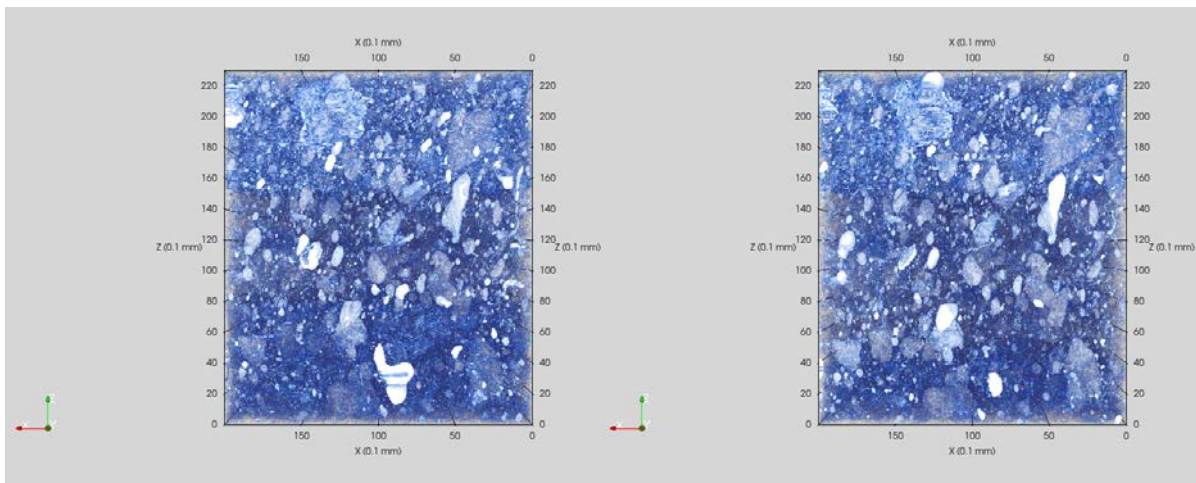


Figure 26. Neutron images of sample DP. (a) Neutron transmission image of uncracked DP sample before water absorption experiment; (b) Neutron transmission image of uncracked DP sample saturated by water due to capillary absorption over 55 minutes (sample was partially immersed in the water at the bottom); (c) Neutron transmission image formed by water only absorbed by the uncracked DP sample over 55 minutes period due to capillary forces; (d) Neutron image of cracked DP sample before water absorption experiment; (e) Neutron image of cracked DP sample at water absorption of 16 minutes (sample was partially immersed in the water at the bottom); (f) Neutron transmission image due to attenuation of water only in cracked DP sample after water absorption of 16 minutes. The grayscale bar indicates the measured neutron transmission integrated over all energies.

Neutron image was taken on the uncracked DP before the water absorption experiment (Fig. 26 (a)). Then, uncracked DP was partially immersed in water at the bottom for 55 minutes and a second neutron image (Fig. 26. b) was taken. Neutron transmission image formed by water attenuation alone, in uncracked DP (Fig. 26. c), was obtained by normalizing the image of the wet sample (Fig. 26. b) by the image taken in a dry state (Fig. 26. a). For DP after introducing cracks,

the reference neutron image and neutron image of a wet cracked DP were obtained following the same procedure (Figs. 26 d-f).

The comparison between the reference neutron images (Fig. 26. a and b) and the 2D porosity density projection images (Fig. 27. c and d) show their similarity. The flaw regions with high transmission value (light) in neutron images are corresponding to the regions of high porosity density (>0.2) in projection images. This observation again implies the correctness of image segmentation results. After its absorption, water is homogeneously distributed in the uncracked DP sample (Fig. 26. c) and fills the majority of pores. In comparison, there is less water in regions (e.g., in the upper right corner of Fig. 26. f) with high porosity density (Fig. 27. d).



(a)

(b)

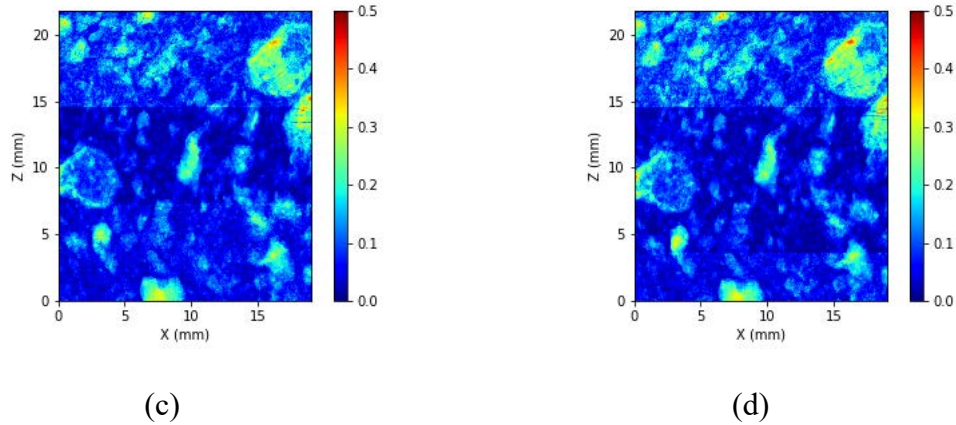


Figure 27. 2D view (XZ plane) of segmented pore phase for (a) uncracked DP sample and (b) cracked DP sample. 2D porosity projection (XZ plane) of (c) porosity density in uncracked DP sample and (d) porosity density in cracked DP sample. Plots (c) and (d) are projected from plots (a) and (b) along Y-axis. The porosity density value at each pixel is defined as the number of pore voxels divided by the total number of voxels along Y-axis during the projection.

Neutron images were taken at constant interval times (typically multiple times per second) from the beginning of water absorption experiments; thus, the process of water absorption of DP sample before and after introducing cracks can be visualized. This process provided the flexibility of using different time scales during data analysis. Water attenuation images for the uncracked DP (Fig. 28) correspond to an image integration time of 104 seconds, with every other image (208 seconds apart) shown in that figure. For the faster process of water penetration observed for the cracked DP sample, visualized in Fig. 29, the image integration time was chosen at 38.5 sec, with every other image (separated by 77 sec) shown in that figure as well.

Neutron images clearly present both the rise of water level and water penetration along the horizontal direction (x-axis). For the uncracked DP, the water level rose relatively evenly on the horizontal line as shown in Fig. 28, although the pores are not evenly distributed along in the horizontal direction, as shown in Fig. 27 (a) and (c).

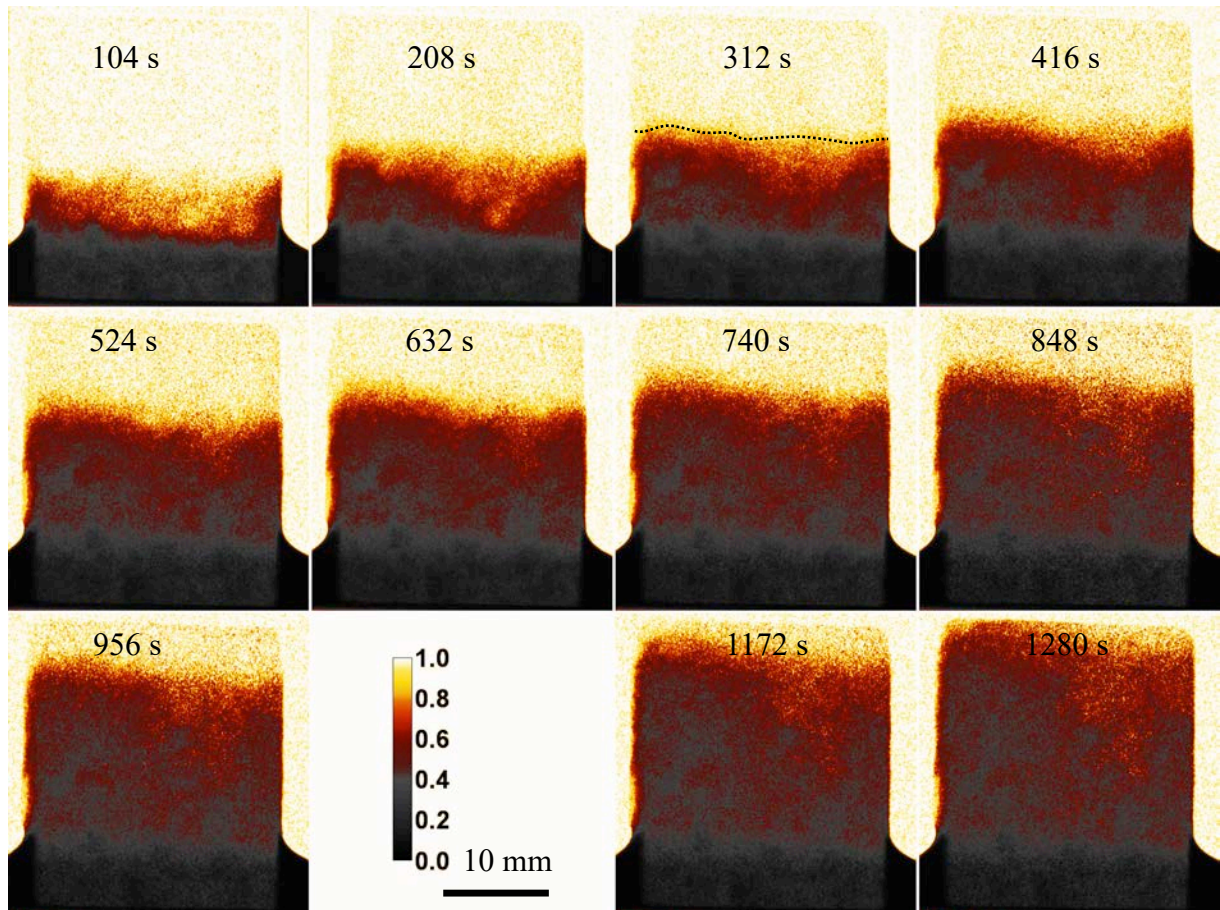


Figure 28. Neutron transmission images of uncracked DP during water absorption due to capillary forces. Only attenuation by water is shown (contribution of concrete is removed by normalization by the image taken with the dry sample). Consecutive images taken with an interval time of 208 s are shown (integration time per image 104 sec). The front of water penetration is shown by the dashed line in one of the images. The image at 1064 s is absent due to the interruption of neutron beam production.

Fig. 29 shows the uptake of water in cracked DP. Because multiple macro and micro cracks have been introduced by compression, the uptake of water in cracked DP is faster than in uncracked DP. Instead of rising evenly on the horizontal line, the water level in cracked DP rose much faster in the regions where cracks propagated and formed fracture planes (Fig. 13 (d) and Fig. 14 (f)) than the regions without cracks. Considering the 3D rendering of connected porosity in cracked DP sample, this result indicates that the rate of water uptake is strongly correlated with the connected pore/crack networks rather than the isolated pores.

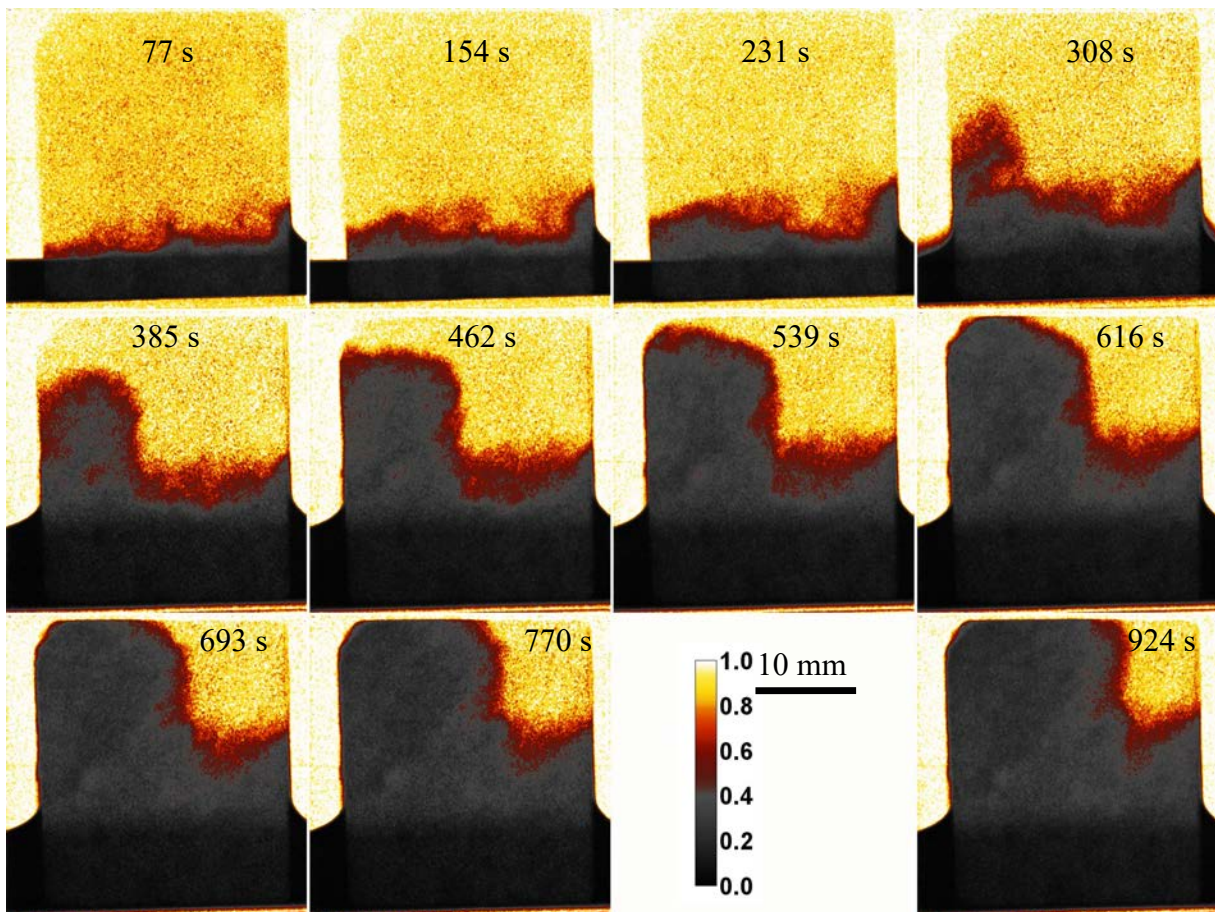
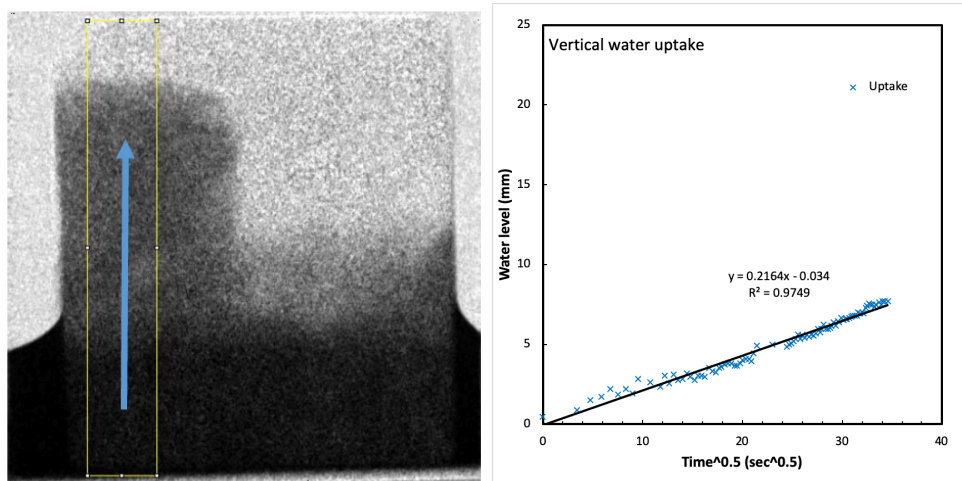
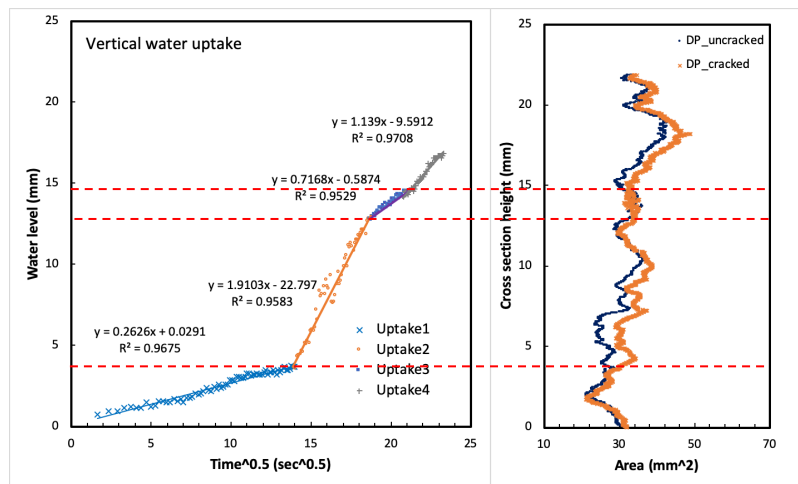


Figure 29. Neutron images and water distributions of cracked DP with an interval time of 77 s respectively. The integration time per image is of 38.5 sec.



(a)

(b)



(c)

(d)

Figure 30. Correlation between the rate of water uptake and cross section area of pores along the height. Water level versus sqrt of water absorption time in (a) Location of areas along which the dynamics of water absorption is shown in the graphs (b) and (c), (b) uncracked DP sample, (c) cracked DP sample, (d) Total cross section area of pores given by μ CT along the height of sample DP.

From the qualitative understanding of the images, previous discussions indicate that the connected pore network plays an important role in the rate of water uptake. Here, Fig. 30 quantitatively evaluates the relationship between the water uptake rate and the cross-sectional area of pores along with the sample height, as follows. Water levels during the water absorption experiments were manually measured using Fiji. For Fig. 30 (d), the total areas of the pore phase along the height are calculated based on the μ CT image segmentation results. The water level (absorption depth) h , as a function of time t , can be predicted for an ideal capillary absorption by means of the Eq. 1 (Note the limitation for h : at a certain height, the water column gravity will equalize the capillary force and water level will stop rising).

$$h(t) = Bt^{1/2} \quad (1)$$

where B is the coefficient of capillary penetration (sorptivity). In both Figs.30 (a) and (b), linear regression and segmented regression (four segments) fitted well the dataset $(t^{1/2}, h)$ with a coefficient of determination over 95%. Therefore, the coefficient of capillary penetration B can be approximated as the slope of each curve segment $(t^{1/2}, h)$. For the uncracked sample, the slope of the curve was nearly constant during the whole experiment, even though the area of pores varied along the height. However, the introduced cracks critically influenced the gradients of segmented curves. As shown in Fig. 30.c, the gradient coefficient B of Uptake1 curve ($h < 5$ mm) was similar to the gradient of the uncracked sample. When the water level rose to 3 mm, B was dramatically increased from $0.26 \text{ mm}/\sqrt{s}$ to $1.91 \text{ mm}/\sqrt{s}$ due to reaching the region of cracks. The areas of newly introduced cracks were less than 25% of the areas of original pores. This quantitative analysis indicates again that the connected pore/crack networks rather than the isolated pores play an important role in determining the rate of water uptake.

3.3.4 Dynamics of water absorption in dry Pompeii sample after introducing cracks

The dynamic water absorption experiment on the uncracked WP was not conducted since the sample was originally wet. After a first neutron radiography test (to get a reference state), the uncracked WP sample was scanned using μ CT and dried out. Then, cracks were introduced into the WP sample. The dynamic water absorption experiment was conducted on an initially dry cracked WP sample.

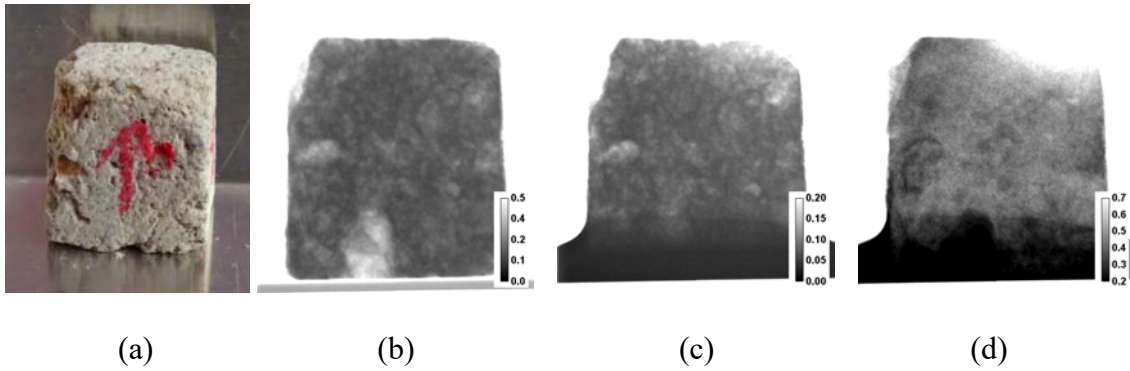


Figure 31. (a) Photograph of dried and cracked WP sample before water absorption experiment (b) Neutron transmission image of cracked dried WP sample before water absorption experiment, (c) Neutron transmission image of cracked WP sample after water absorption over 11 minutes period, (d) Neutron image of only water in cracked WP sample after water absorption.

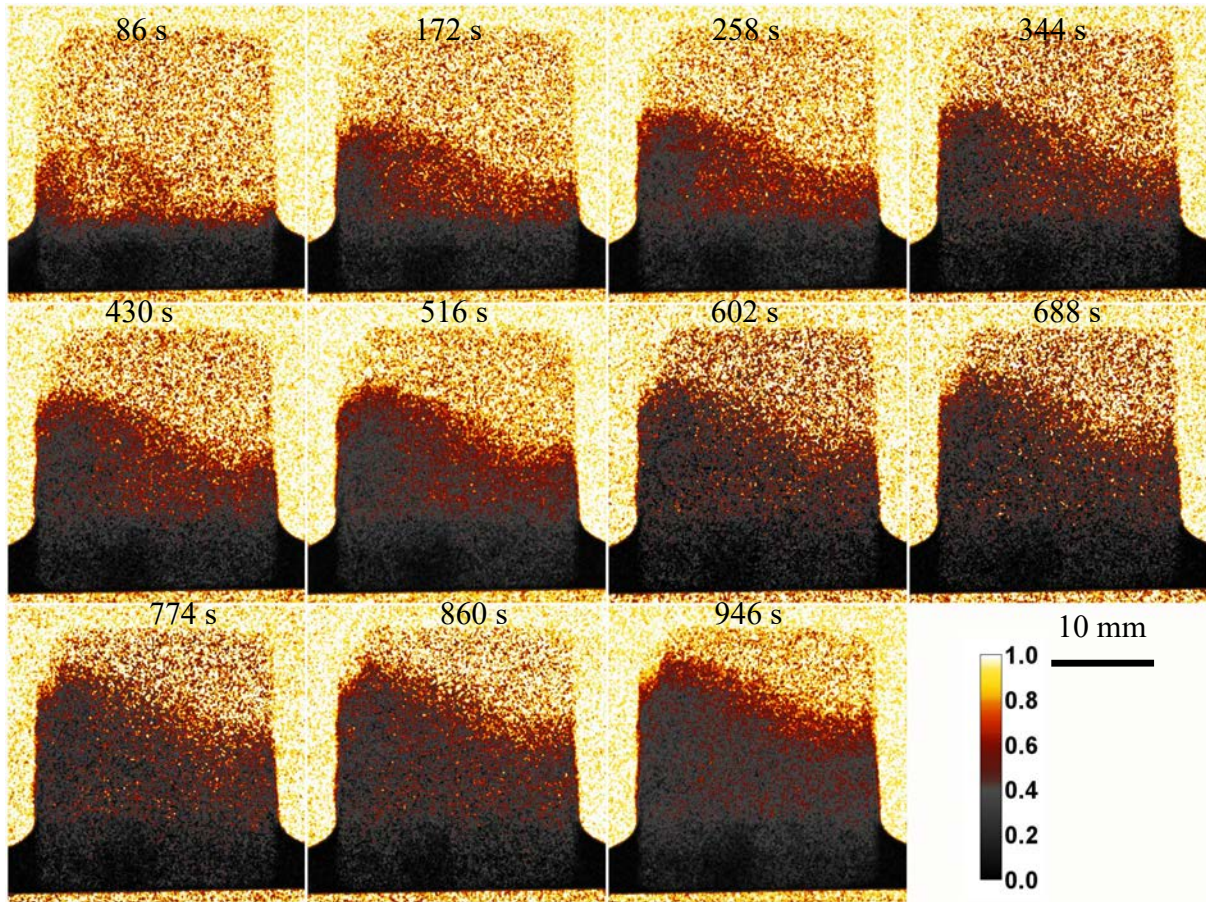


Figure 32. Neutron images of water distribution within cracked WP taken with an interval time of 86 s.

Fig. 32 shows the uptake of water in the cracked WP sample. The uptake of water on the left-hand side was faster than the right-hand side. The water level in cracked DP sample rose much faster in the region $\{X, Z: 0 \text{ mm} \leq X \leq 10 \text{ mm}, 0 \text{ mm} \leq Z \leq 25 \text{ mm}\}$ (where cracks propagated and formed fracture planes (Fig. 15 (f) and Fig. 16 (f))) than in the regions without cracks. Considering the 3D rendering of connected porosity in cracked WP sample (Fig. 17 d), this result confirms that the rate of water uptake is more strongly correlated with the connected pore/crack networks rather than with the isolated pores.

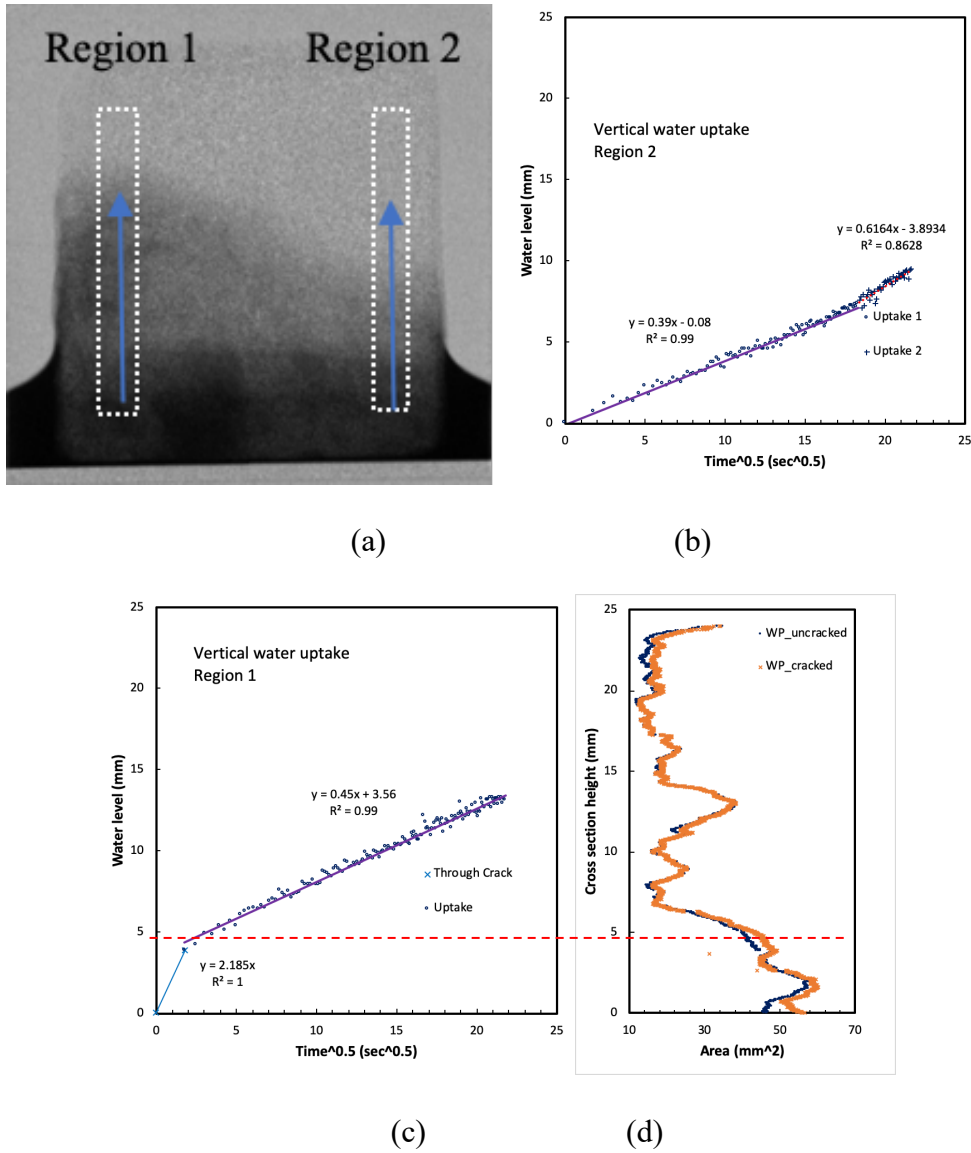


Figure 33. Correlation between the rate of water uptake and the cross-sectional area of pores along the height of the cracked WP sample. Water level versus sqrt of water absorption time in (a) Location of areas along which the dynamics of water absorption are shown in the graphs (b) and (c) for regions 2 and 1, respectively. Note that water level in (b) and (c) start at ~10 mm above the sample bottom. (d) Total cross-sectional area of pores along the height of the sample WP.

Similar to DP, Fig. 33 provides a quantitative evaluation of the relations between the water uptake rate and the cross-sectional area of pores along the sample height for cracked WP sample. For the water uptake on the left-hand side (region 1), the coefficient of capillary penetration (B) is 2.19 mm/ \sqrt{s} at first ($h < 5\text{mm}$) due to the introduced macro cracks and to the connected large pore network at the bottom of Region 1. However, B is 0.39 mm/ \sqrt{s} at the bottom of Region 2 for the same WP sample. This is close to the value of uncracked sample DP, meaning that this part of water flux is controlled by similar pore systems. Because of the 3D rendering of connected objects for the pore phase in Fig. 17 and the significant difference in pore area below 5mm in Fig. 33 (d), the results indicate that both connectivity and volume at the bottom of Region 1 increased after cracking, while the pores in Region 2 preserve their connectivity and size. The macro cracks only initiated and propagated in Region 1 of WP.

In summary, the local microstructural information, such as the presence of cracks and the increase of regional pore connectivity, has a significant influence on the water uptake rate. This fact increases the local coefficient of capillary penetration in ancient Pompeii samples. Between the cracked and uncracked regions, the local coefficient of capillary penetration B is different by one order of magnitude. Since this coefficient is proportional to the critical pore size (Eq. 2), through which water penetrates by capillary suction, the order of magnitude difference means that the pore size controlling water uptake is possibly one order of magnitude smaller in uncracked concrete compared to cracked material (Table 6).

3.4 Comparison of the results

3.4.1 Porosity and connectivity

In the literature, the 3D structures of paste and concrete have been widely studied by X-ray microtomography [72]. Calculated porosity and connectivity vary as a function of mixture design, voxel resolution, segmentation method, and other minor factors. Using 3D μ CT of cement paste with different resolutions, Gallucci et al. [73] reported that an increase in voxel size (i.e., decrease in resolution) (from 0.67 to 1.34, 2 and 2.67 μm respectively) induces a decrease in calculated porosity (from 18.60 to 11.48, 6.63, and 5.03 % respectively) and in calculated pore connectivity (from 95% to 82, 66 and 0). Table 4 lists the porosity and pore connectivity of typical cementitious materials calculated from microtomography data. Voxel sizes range from 1 μm to 15 μm , and grey level threshold methods were applied for the phase segmentation.

The porosity of the paste alone for the ancient Pompeii sample was calculated from segmented μ CT images. The porosity of ancient Pompeii paste was defined as the volume of pores surrounded by paste (matrix) divided by the sum of the paste (matrix)'s volume and the volume of pores surrounded by paste (matrix). On the other hand, the aggregate phase and pore phase within the aggregates were not counted for the calculation of paste porosity. To separate the aggregates and pores within the aggregates from the objects of other phases (matrix and pore connected to matrix), the voxels of pores surrounded by the aggregates merged into the voxels of surrounding aggregates using the hole filling algorithm in Fiji. Then the voxels of merged aggregated phase were deleted from the whole segmented dataset, and only the voxels of paste (matrix) phase and the voxels of pore which connected to paste (matrix) phase were left to calculate the porosity in paste.

Table 4. A comparison of porosity for different concretes from microtomography (PC: Portland cement, SHCC: strain hardening cement composites).

Material	Cement paste volume (% total volume)	Porosity	Pore connectivity (% of total porosity)	Voxel size (um)
uncracked DP concrete	79	8.68%	0% (9.37%)	9.5
uncracked DP paste	100	9.51%	-	9.5
uncracked WP concrete	62	13.48%	0% (31.48%)	9.5
uncracked WP paste	100	16.74%	-	9.5
PC paste (W/C=0.25) [74]	100	1.36% [74]	-	5.0 [74]
PC paste (W/C=0.5) [73] [46]	100 [73], 100 [46]	1.28% [73], 1.8% [46]	-, 14% [46]	5.0 [73], 1.8 [46]
PC concrete (W/C=0.35) [75]	~ 51 [75]	2.87% [75]	-	15.2 [75]
PC concrete (W/C=0.5) [76]	~ 46 [76]	6.50% [76]	-	6.18 [76]
PC SHCC [77]	77-87 [77]	2.4% - 3% [77]	-	4.8 [77]

As shown in Table 4, the ancient Pompeii samples have much larger porosities when comparing with other typical Portland cement materials even if the voxel size of ancient Pompeii samples is relatively larger. The porosities of ancient Pompeii paste and concrete are a magnitude greater than the porosities of paste and concrete with low W/C. Note that the pore network connectivity of the DP sample is lower than that of PC paste with a w/c ratio of 0.5, although the DP sample shows a much higher porosity.

From MIP results, the total porosity of ancient Pompeii samples ranges from 34.5% to 36.2%. The porosity of DP sample from microtomography is 8.86%, which means that microtomography

successfully detected the largest pores, which represent ~ 25% of the whole pore volume. This result is consistent with other studies that microtomography only provides partial quantification of the pore system of a concrete. Due to its resolution (voxel size of 9.5 microns), microtomography is not able to detect the smallest pores (below 19 microns i.e., below the size of two voxels), although they represent up to 70-90% of the whole pore volume of cement paste, according to the MIP results [46, 78]. 3D FIB/SEM is capable of reaching pores down to tens of nm [66], and in the case of modern HPC, pores of tens of nm percolate significantly through the paste.

3.4.2 Coefficient of capillary penetration

Table 5. A comparison of capillary penetration coefficient (B) for different concretes from neutron radiography (unit: mm/min^{1/2}).

Material	Cement paste volume (% total volume)	B of uncracked sample	B of cracked sample
DP concrete	79	1.67	2.03 – 14.80
WP concrete	62	3.02	3.48 – 16.92
PC mortar (W/C=0.36)	35 [79]	1.57 [79]	-
PC mortar (W/C=0.4)	27 [80]	0.39-0.61 [80]	-
PC mortar (W/C=0.42)	35 [79]	2.24 [79]	-
PC mortar (W/C=0.5)	35 [79]	2.38 [79]	-
PC mortar (W/C=0.6)	30 [80]	1.16 [80]	-
PC concrete (W/C=0.4)	24 [81]	0.89 [81]	-
PC concrete (W/C=0.6)	24 [81]	1.43 [81]	-
PC SHCC	63 [82]	1.14 [82]	-

When comparing the capillary penetration coefficient B of ancient Pompeii samples and conventional cement materials in Table 5, it is interesting to see that the capillary penetration coefficient of DP and WP are similar to modern Portland-based reference cement materials, although the porosity of ancient Pompeii sample is much higher. Therefore, the porous ancient

Pompeii mortar/concrete has comparable capillary penetration rate to modern Portland cement materials, and the capillary penetration rate is key to the resistance to long term erosion of water and to improved durability. Similar water penetration rates also mean that the percolating pore systems of both ancient Pompeii and modern Portland-cement based materials have similar pore sizes, and these are the pores controlling fluid ingress, permeability, and durability.

3.4.3 Permeability prediction

Capillary penetration coefficient B is related to a critical pore size d_c by Washburn equation:

$$B = \sqrt{\frac{\gamma d_c \cos(\phi)}{4\eta}} \quad (2)$$

Where, γ is the interface surface tension, η is the dynamic viscosity, and ϕ is the contact angle. For undamaged ancient Pompeii concrete, critical pore sizes d_c , corresponding to the measured penetration coefficients B , are on the order of 2.6-8.2 nm (Table 6).

Table 6. Prediction of critical pore sizes using Washburn equation, along the Z-axis (vertical) direction. Assuming at room temperature (25 °C), water/cement/air interface surface tension γ is 66 mN/m [83], dynamic viscosity η of water is 0.89 mPa.s, and $\cos(\phi)$ is 1 (water is a perfectly wetting fluid) [84].

Sample	B (mm/ \sqrt{s})	d_c (nm)
uncracked DP sample	0.22	2.6
cracked DP sample	0.26-1.91	3.8-196.8
cracked WP sample	0.39-2.19	8.2-258

These values are consistent with the typical pore sizes of modern Portland cement paste hydrates (C-A-S-H) [64]. They also describe the main channels for water flow, i.e. they describe a percolating pore system.

In a first approach, a 1D Katz-Thompson equation [68] is able to describe fluid permeability K as a function of a critical pore size d_c , characteristic of fluid percolation, as:

$$K = \frac{d_c^2 \phi_{percolating}}{226\tau} \quad (3)$$

This yields the following values (Table 7) for K , on the order of 10^{-20} - 10^{-19} m² for ancient Pompeii concrete with the d_c from Table 6. Such values correspond to that of highly durable modern Portland concretes [66, 85], explaining the actual durability of ancient Pompeii concrete. Besides, the predicted K varied with d_c from different measurements. Further experiment for permeability measurement is required.

Table 7. Prediction of fluid permeability using Katz-Thompson equation, along the Z-axis (vertical) direction, for uncracked Pompeii sample.

Sample	Porosity	d_c (nm)	Tortuosity	K (m ²)
uncracked Pompeii mortar fragments	34.5%-36.2%	770-860 (MIP)		$6.9-9.5 \text{ e}^{-16}$
uncracked DP sample	(MIP)	20-40 (modern PC)	1.25-1.32	$4.6 \text{ e}^{-18}-2.1 \text{ e}^{-17}$
cracked DP sample		2.6 (neutron)	(μ CT)	$1.0-1.2 \text{ e}^{-20}$
cracked WP sample		3.8-196.8 (neutron)		$1.9 \text{ e}^{-20}-4.9 \text{ e}^{-17}$
		8.2-258 (neutron)		$7.8 \text{ e}^{-20}-8.5 \text{ e}^{-17}$

For cracked Pompeii concrete however, a Poiseuille law (Eq. 4, where h_{min} is the minimum width of the percolating pore/crack) [86] is more adapted, see Table 8. This yields permeability values greater by several orders of magnitude than that of undamaged concrete.

$$K = \frac{h_{min}^2}{12} \quad (4)$$

Table 8. Prediction of fluid permeability using Poiseuille law, along the Z-axis (vertical) direction, for cracked Pompeii sample.

Sample	h_{min} (μm)	K (m^2)
cracked Pompeii concrete	19-100 (μCT)	3.0 e^{-11} - 8.3 e^{-10}

4. Conclusions

The integrated synchrotron X-ray μCT and neutron radiography with computer vision analysis is a powerful non-destructive testing method to conduct a systematic investigation on the complex concrete microstructure and the dynamics of water penetration. Synchrotron X-ray microtomography provides high-resolution 3D microtomography images with a broad field of view. After the reconstruction of the μCT image, machine learning-based image segmentation methods, and DVC analysis achieved both qualitative and quantitative microstructural information from the ancient Pompeii concrete sample. An innovative pipeline was developed to process the large datasets autonomously. The phase segmentation results using the Random Forest classifier were of relatively high accuracy. Segmented pore and aggregate phases were visualized in 3D rendering. The multiple micro and macro cracks propagations and wider dispersion of cracks in both dry and wet Pompeii samples were observed, which presented a stable and ductile fracture pattern. 3D morphological and statistical microstructure analysis from the accurate segmented microtomography image provides 3D pore network information such as porosity, pore size distribution, and pore connectivity, explaining the difference of water uptake rates at different meso-structural regions in dynamic neutron radiography experiments.

The experimental results show that the water penetration rate highly depends on the local microstructure such as regional pore connectivity and the presence of cracks while it depends less on the global microstructural information such as global porosity. For uncracked ancient Pompeii samples, the water capillary penetration coefficient (1.67 and 3.02 mm/min^{1/2}) in both dry and wet samples are comparable to modern PC paste/concrete (ranging from 0.39 to 2.38 mm/min^{1/2}), while ancient Pompeii concrete (8.86% and 18.22% for dry and wet sample based on microtomography, and ranging from 34.5% to 36.2% based on MIP) is more porous than modern PC paste/concrete (W/C = 0.5, ranging from 1.28% to 6.50% based on microtomography, and ranging from 27% to 31% based on MIP [78, 87]). Note that the porosity calculated from microtomography here ignored the smallest pores that represent ~ 75% of the whole pore volume. After introducing cracks, the global porosity for both samples are nearly the same, but the pore connectivity increased. The pores get connected by the introduced cracks and merged into more elongated pore networks. Instead of being a constant, the water uptake rate and capillary penetration coefficient varied depending on the local microstructure. The capillary penetration coefficient in regions with cracks propagations increased significantly (>10 mm/min^{1/2}) while the capillary penetration coefficient in the uncracked regions remains similar. Although further experiment for permeability measurement is required, the predicted permeability of uncracked Pompeii samples based on 1D Katz-Thompson model and Washburn equation ranges from 10⁻²⁰ to 10⁻¹⁹ m², which correspond to that of highly durable modern Portland concretes.

The high durability of porous ancient Pompeii concrete is benefited from the ductile fracture pattern and low connectivity in the pore network. The integrated synchrotron X-ray

microtomography and neutron radiography with computer vision analysis is a step forward in the understanding of the durability of ancient Pompeii concrete and other complex cement materials.

Acknowledgements

This work was supported by the SusChEM program, Grant No. DMR-1410557, and the Division of Materials Research Ceramics Program, DMR-CER, Grant No.1935604 of National Science Foundation. This research used resources of the Advanced Light Source, a U.S. DOE Office of Science User Facility under contract no. DE-AC02-05CH11231. The authors thank Dilworth Parkinson for assistance with the μ CT experiments. We also acknowledge the access to neutron imaging facility at JPARC and the great help of our colleagues Dr. T. Shinohara and K. Oikawa with neutron imaging experiments. These neutron experiments at the Materials and Life Science Experimental Facility of the J-PARC were performed under a user program (Proposal No. 2016B0183).

References

- [1] M.D. Jackson, J. Moon, E. Gotti, R. Taylor, S.R. Chae, M. Kunz, A.H. Emwas, C. Meral, P. Guttman, P. Levitz, Material and elastic properties of Al-tobermorite in ancient Roman seawater concrete, *Journal of the American Ceramic Society*, 96 (2013) 2598-2606.
- [2] M.D. Jackson, S.R. Mulcahy, H. Chen, Y. Li, Q. Li, P. Cappelletti, H.-R. Wenk, Phillipsite and Al-tobermorite mineral cements produced through low-temperature water-rock reactions in Roman marine concrete, *American Mineralogist*, 102 (2017) 1435-1450.

- [3] M.D. Jackson, S.R. Chae, S.R. Mulcahy, C. Meral, R. Taylor, P. Li, A.-H. Emwas, J. Moon, S. Yoon, G. Vola, Unlocking the secrets of Al-tobermorite in Roman seawater concrete, *American Mineralogist*, 98 (2013) 1669-1687.
- [4] T. Vanorio, W. Kanitpanyacharoen, Rock physics of fibrous rocks akin to Roman concrete explains uplifts at Campi Flegrei Caldera, *Science*, 349 (2015) 617-621.
- [5] A. Palomo, P. Monteiro, P. Martauz, V. Bílek, A. Fernandez-Jimenez, Hybrid binders: A journey from the past to a sustainable future (opus caementicium futurum), *Cement and Concrete Research*, 124 (2019) 105829.
- [6] M.D. Jackson, E.N. Landis, P.F. Brune, M. Vitti, H. Chen, Q. Li, M. Kunz, H.-R. Wenk, P.J. Monteiro, A.R. Ingraffea, Mechanical resilience and cementitious processes in Imperial Roman architectural mortar, *Proceedings of the National Academy of Sciences*, 111 (2014) 18484-18489.
- [7] P. Trtik, B. Münch, W.J. Weiss, A. Kaestner, I. Jerjen, L. Josic, E. Lehmann, P. Lura, Release of internal curing water from lightweight aggregates in cement paste investigated by neutron and X-ray tomography, *Nuclear Instruments and Methods in Physics Research Section A: Accelerators, Spectrometers, Detectors and Associated Equipment*, 651 (2011) 244-249.
- [8] P. Zhang, F.H. Wittmann, P. Lura, H.S. Müller, S. Han, T. Zhao, Application of neutron imaging to investigate fundamental aspects of durability of cement-based materials: A review, *Cement and Concrete Research*, 108 (2018) 152-166.
- [9] T. Pescatore, M.R. Senatore, G. Capretto, G. Lerro, Holocene coastal environments near Pompeii before the AD 79 eruption of Mount Vesuvius, Italy, *Quaternary Research*, 55 (2001) 77-85.

- [10] D. Silva, H. Wenk, P. Monteiro, Comparative investigation of mortars from Roman Colosseum and cistern, *Thermochimica Acta*, 438 (2005) 35-40.
- [11] A. Telesca, M. Marroccoli, M. Pace, M. Tomasulo, G. Valenti, P. Monteiro, A hydration study of various calcium sulfoaluminate cements, *Cement and Concrete Composites*, 53 (2014) 224-232.
- [12] A. Tremsin, High resolution neutron counting detectors with microchannel plates and their applications in neutron radiography, diffraction and resonance absorption imaging, *Neutron News*, 23 (2012) 35-38.
- [13] A. Tremsin, J. Vallergera, J. McPhate, O. Siegmund, Optimization of high count rate event counting detector with Microchannel Plates and quad Timepix readout, *Nuclear Instruments and Methods in Physics Research Section A: Accelerators, Spectrometers, Detectors and Associated Equipment*, 787 (2015) 20-25.
- [14] A. Tremsin, J. Vallergera, Unique capabilities and applications of Microchannel Plates detectors with Medipix/Timepix readout, *Radiation Measurements*, (2019) 106228.
- [15] A. Tremsin, T. Shinohara, K. Oikawa, J. Li, P. Monteiro, Non-destructive mapping of water distribution through white-beam and energy-resolved neutron imaging, *Nuclear Instruments and Methods in Physics Research Section A: Accelerators, Spectrometers, Detectors and Associated Equipment*, 927 (2019) 174-183.
- [16] A. MacDowell, D. Parkinson, A. Haboub, E. Schaible, J. Nasiatka, C. Yee, J. Jameson, J. Ajo-Franklin, C. Brodersen, A. McElrone, X-ray micro-tomography at the Advanced Light Source, *Developments in X-Ray Tomography VIII*, International Society for Optics and Photonics, 2012, pp. 850618.

- [17] D. Gürsoy, F. De Carlo, X. Xiao, C. Jacobsen, TomoPy: a framework for the analysis of synchrotron tomographic data, *Journal of synchrotron radiation*, 21 (2014) 1188-1193.
- [18] W. Kanitpanyacharoen, D.Y. Parkinson, F. De Carlo, F. Marone, M. Stampanoni, R. Mokso, A. MacDowell, H.-R. Wenk, A comparative study of X-ray tomographic microscopy on shales at different synchrotron facilities: ALS, APS and SLS, *Journal of synchrotron radiation*, 20 (2013) 172-180.
- [19] J. Schindelin, I. Arganda-Carreras, E. Frise, V. Kaynig, M. Longair, T. Pietzsch, S. Preibisch, C. Rueden, S. Saalfeld, B. Schmid, Fiji: an open-source platform for biological-image analysis, *Nature methods*, 9 (2012) 676-682.
- [20] D. Ushizima, D. Parkinson, P. Nico, J. Ajo-Franklin, A. MacDowell, B. Kocar, W. Bethel, J. Sethian, Statistical segmentation and porosity quantification of 3d x-ray microtomography, *Applications of Digital Image Processing XXXIV*, International Society for Optics and Photonics, 2011, pp. 813502.
- [21] B.D. Levin, Y. Jiang, E. Padgett, S. Waldon, C. Quammen, C. Harris, U. Ayachit, M. Hanwell, P. Ercius, D.A. Muller, Tutorial on the visualization of volumetric data using tomviz, *Microscopy Today*, 26 (2018) 12-17.
- [22] Z. Yang, W. Ren, R. Sharma, S. McDonald, M. Mostafavi, Y. Vertyagina, T. Marrow, In-situ X-ray computed tomography characterisation of 3D fracture evolution and image-based numerical homogenisation of concrete, *Cement and Concrete Composites*, 75 (2017) 74-83.
- [23] H. Zelelew, A. Papagiannakis, A volumetrics thresholding algorithm for processing asphalt concrete X-ray CT images, *International journal of pavement engineering*, 12 (2011) 543-551.
- [24] W.D. Carlson, Three-dimensional imaging of earth and planetary materials, *Earth and Planetary Science Letters*, 249 (2006) 133-147.

- [25] D. Meyer, H.-K. Man, J.G. van Mier, Fracture of foamed cementitious materials: a combined experimental and numerical study, IUTAM Symposium on Mechanical Properties of Cellular Materials, Springer, 2009, pp. 115-123.
- [26] W.J. Shipman, A.L. Nel, D. Chetty, J.D. Miller, C.-L. Lin, The application of machine learning to the problem of classifying voxels in X-ray microtomographic scans of mineralogical samples, 2013 IEEE International Conference on Industrial Technology (ICIT), IEEE, 2013, pp. 1184-1189.
- [27] M. Camalan, M. Çavur, Ç. Hoşten, Assessment of chromite liberation spectrum on microscopic images by means of a supervised image classification, Powder Technology, 322 (2017) 214-225.
- [28] I. Arganda-Carreras, V. Kaynig, C. Rueden, K.W. Eliceiri, J. Schindelin, A. Cardona, H. Sebastian Seung, Trainable Weka Segmentation: a machine learning tool for microscopy pixel classification, Bioinformatics, 33 (2017) 2424-2426.
- [29] T.K. Ho, Random decision forests, Proceedings of 3rd international conference on document analysis and recognition, IEEE, 1995, pp. 278-282.
- [30] R. Caruana, N. Karampatziakis, A. Yessenalina, An empirical evaluation of supervised learning in high dimensions, Proceedings of the 25th international conference on Machine learning, 2008, pp. 96-103.
- [31] D. Ushizima, K. Xu, P.J. Monteiro, Materials Data Science for Microstructural Characterization of Archaeological Concrete, MRS Advances, 1-14.
- [32] F.D.E. Latief, S. Feranie, Three-dimensional visualization and characterization of cracks in geothermal reservoir rock using image analysis of reconstructed μ CT images: A preliminary study, AIP Conference Proceedings, American Institute of Physics, 2014, pp. 120-123.

- [33] C.M. Loeffler, Y. Qiu, B. Martin, W. Heard, B. Williams, X. Nie, Detection and segmentation of mechanical damage in concrete with X-Ray microtomography, *Materials Characterization*, 142 (2018) 515-522.
- [34] J. Schock, S. Liebl, K. Achterhold, F. Pfeiffer, Obtaining the spacing factor of microporous concrete using high-resolution Dual Energy X-ray Micro CT, *Cement and Concrete Research*, 89 (2016) 200-205.
- [35] S. Roux, F. Hild, P. Viot, D. Bernard, Three-dimensional image correlation from X-ray computed tomography of solid foam, *Composites Part A: Applied science and manufacturing*, 39 (2008) 1253-1265.
- [36] C.J. Brandon, R.L. Hohlfelder, M.D. Jackson, J.P. Oleson, *Building for eternity: the history and technology of Roman concrete engineering in the sea*, Oxbow books 2014.
- [37] B.K. Bay, Methods and applications of digital volume correlation, *The Journal of Strain Analysis for Engineering Design*, 43 (2008) 745-760.
- [38] B.K. Bay, T.S. Smith, D.P. Fyhrie, M. Saad, Digital volume correlation: three-dimensional strain mapping using X-ray tomography, *Experimental mechanics*, 39 (1999) 217-226.
- [39] H. Leclerc, J.-N. Périé, F. Hild, S. Roux, Digital volume correlation: what are the limits to the spatial resolution?, *Mechanics & Industry*, 13 (2012) 361-371.
- [40] T. Taillandier-Thomas, S. Roux, T.F. Morgeneyer, F. Hild, Localized strain field measurement on laminography data with mechanical regularization, *Nuclear Instruments and Methods in Physics Research Section B: Beam Interactions with Materials and Atoms*, 324 (2014) 70-79.

- [41] A. Bouterf, J. Adrien, E. Maire, X. Brajer, F. Hild, S. Roux, Failure mechanisms of plasterboard in nail pull test determined by x-ray microtomography and digital volume correlation, *Experimental Mechanics*, 56 (2016) 1427-1437.
- [42] A. Bouterf, S. Roux, F. Hild, J. Adrien, E. Maire, S. Meille, Digital Volume Correlation Applied to X-ray Tomography Images from Spherical Indentation Tests on Lightweight Gypsum, *Strain*, 50 (2014) 444-453.
- [43] B. Münch, L. Holzer, Contradicting geometrical concepts in pore size analysis attained with electron microscopy and mercury intrusion, *Journal of the American Ceramic Society*, 91 (2008) 4059-4067.
- [44] K.L. Scrivener, Backscattered electron imaging of cementitious microstructures: understanding and quantification, *Cement and concrete Composites*, 26 (2004) 935-945.
- [45] K.L. Willis, A.B. Abell, D.A. Lange, Image-based characterization of cement pore structure using wood's metal intrusion, *Cement and Concrete Research*, 28 (1998) 1695-1705.
- [46] N. Bossa, P. Chaurand, J. Vicente, D. Borschneck, C. Levard, O. Aguerre-Chariol, J. Rose, Micro-and nano-X-ray computed-tomography: A step forward in the characterization of the pore network of a leached cement paste, *Cement and Concrete Research*, 67 (2015) 138-147.
- [47] T. Sugiyama, M. Promentilla, T. Hitomi, N. Takeda, Application of synchrotron microtomography for pore structure characterization of deteriorated cementitious materials due to leaching, *Cement and Concrete Research*, 40 (2010) 1265-1270.
- [48] M. Doube, M.M. Klosowski, I. Arganda-Carreras, F.P. Cordelières, R.P. Dougherty, J.S. Jackson, B. Schmid, J.R. Hutchinson, S.J. Shefelbine, BoneJ: free and extensible bone image analysis in ImageJ, *Bone*, 47 (2010) 1076-1079.

- [49] O.A. HJG, Gundersen, Quantification of connectivity in cancellous bone, with special emphasis on 3-d reconstruction, *Bone*, 14 (1993) 173-182.
- [50] J. Toriwaki, T. Yonekura, Euler number and connectivity indexes of a three dimensional digital picture, *FORMA-TOKYO-*, 17 (2002) 183-209.
- [51] T.-C. Lee, R.L. Kashyap, C.-N. Chu, Building skeleton models via 3-D medial surface axis thinning algorithms, *CVGIP: Graphical Models and Image Processing*, 56 (1994) 462-478.
- [52] I. Arganda-Carreras, R. Fernández-González, A. Muñoz-Barrutia, C. Ortiz-De-Solorzano, 3D reconstruction of histological sections: Application to mammary gland tissue, *Microscopy research and technique*, 73 (2010) 1019-1029.
- [53] N.R. Backeberg, F. Iacoviello, M. Rittner, T.M. Mitchell, A.P. Jones, R. Day, J. Wheeler, P.R. Shearing, P. Vermeesch, A. Striolo, Quantifying the anisotropy and tortuosity of permeable pathways in clay-rich mudstones using models based on X-ray tomography, *Scientific reports*, 7 (2017) 1-12.
- [54] H. Loosveldt, Z. Lafhaj, F. Skoczylas, Experimental study of gas and liquid permeability of a mortar, *Cement and concrete research*, 32 (2002) 1357-1363.
- [55] M.D. Jackson, J.M. Logan, B.E. Scheetz, D.M. Deocampo, C.G. Cawood, F. Marra, M. Vitti, L. Ungaro, Assessment of material characteristics of ancient concretes, Grande Aula, Markets of Trajan, Rome, *Journal of Archaeological Science*, 36 (2009) 2481-2492.
- [56] R.J. Myers, E. L'Hôpital, J.L. Provis, B. Lothenbach, Effect of temperature and aluminium on calcium (alumino) silicate hydrate chemistry under equilibrium conditions, *Cement and Concrete Research*, 68 (2015) 83-93.

- [57] R. Hay, J. Li, K. Celik, Influencing factors on micromechanical properties of calcium (alumino) silicate hydrate C-(A-) SH under nanoindentation experiment, *Cement and Concrete Research*, 134 (2020) 106088.
- [58] M. Murat, Stabilité thermique des aluminates de calcium hydratés et phases apparentées, Caractérisation par les méthodes thermoanalytiques. Aluminates Calcium, Int Semin, Turin, Italy, (1982) 59-84.
- [59] M. SAKIZCI, INVESTIGATION OF THERMAL AND STRUCTURAL PROPERTIES OF NATURAL AND ION-EXCHANGED ANALCIME, *Anadolu University of Sciences & Technology-A: Applied Sciences & Engineering*, 17 (2016).
- [60] G. Leone, A. De Vita, A. Magnani, C. Rossi, Characterization of archaeological mortars from Herculaneum, *Thermochimica Acta*, 624 (2016) 86-94.
- [61] A. Moropoulou, K. Polikreti, A. Bakolas, P. Michailidis, Correlation of physicochemical and mechanical properties of historical mortars and classification by multivariate statistics, *Cement and concrete research*, 33 (2003) 891-898.
- [62] J. Li, G. Geng, R. Myers, Y.-S. Yu, D. Shapiro, C. Carraro, R. Maboudian, P.J. Monteiro, The chemistry and structure of calcium (alumino) silicate hydrate: a study by XANES,ptychographic imaging, and wide-and small-angle scattering, *Cement and Concrete Research*, 115 (2019) 367-378.
- [63] H. Binici, S. Kapur, The physical, chemical, and microscopic properties of masonry mortars from Alhambra Palace (Spain) in reference to their earthquake resistance, *Frontiers of Architectural Research*, 5 (2016) 101-110.

- [64] P.J. McDonald, V. Rodin, A. Valori, Characterisation of intra-and inter-C–S–H gel pore water in white cement based on an analysis of NMR signal amplitudes as a function of water content, *Cement and Concrete Research*, 40 (2010) 1656-1663.
- [65] K.L. Scrivener, A. Nonat, Hydration of cementitious materials, present and future, *Cement and concrete research*, 41 (2011) 651-665.
- [66] Y. Song, C. Davy, D. Troadec, X. Bourbon, Pore network of cement hydrates in a high performance concrete by 3D FIB/SEM—implications for macroscopic fluid transport, *Cement and Concrete Research*, 115 (2019) 308-326.
- [67] A. ASTM, ASTM C39/C39M-18: Standard test method for compressive strength of cylindrical concrete specimens, ASTM International, West Conshohocken, PA. ASTM, AI (2018)." ASTM C, 192 (2018).
- [68] G.W. Scherer, J.J. Valenza II, G. Simmons, New methods to measure liquid permeability in porous materials, *Cement and concrete research*, 37 (2007) 386-397.
- [69] S. Diamond, Mercury porosimetry: an inappropriate method for the measurement of pore size distributions in cement-based materials, *Cement and concrete research*, 30 (2000) 1517-1525.
- [70] K. Xu, J.-f. Daian, D. Quenard, Multiscale structures to describe porous media part I: theoretical background and invasion by fluids, *Transport in porous media*, 26 (1997) 51-73.
- [71] A. Tremsin, T. Shinohara, T. Kai, M. Ooi, T. Kamiyama, Y. Kiyonagi, Y. Shiota, J. McPhate, J. Vallerger, O. Siegmund, Neutron resonance transmission spectroscopy with high spatial and energy resolution at the J-PARC pulsed neutron source, *Nuclear Instruments and Methods in Physics Research Section A: Accelerators, Spectrometers, Detectors and Associated Equipment*, 746 (2014) 47-58.

- [72] S. Brisard, M. Serdar, P.J. Monteiro, Multiscale X-ray tomography of cementitious materials: A review, *Cement and Concrete Research*, 128 (2020) 105824.
- [73] E. Gallucci, K. Scrivener, A. Groso, M. Stampanoni, G. Margaritondo, 3D experimental investigation of the microstructure of cement pastes using synchrotron X-ray microtomography (μ CT), *Cement and Concrete Research*, 37 (2007) 360-368.
- [74] U. Rattanasak, K. Kendall, Pore structure of cement/pozzolan composites by X-ray microtomography, *Cement and concrete research*, 35 (2005) 637-640.
- [75] Y.-S. Wang, J.-G. Dai, X-ray computed tomography for pore-related characterization and simulation of cement mortar matrix, *NDT & E International*, 86 (2017) 28-35.
- [76] K.Y. Kim, T.S. Yun, K.P. Park, Evaluation of pore structures and cracking in cement paste exposed to elevated temperatures by X-ray computed tomography, *Cement and Concrete Research*, 50 (2013) 34-40.
- [77] R. Lorenzoni, I. Curosu, S. Paciornik, V. Mechtcherine, M. Oppermann, F. Silva, Semantic segmentation of the micro-structure of strain-hardening cement-based composites (SHCC) by applying deep learning on micro-computed tomography scans, *Cement and Concrete Composites*, 108 (2020) 103551.
- [78] R.A. Cook, K.C. Hover, Mercury porosimetry of hardened cement pastes, *Cement and Concrete research*, 29 (1999) 933-943.
- [79] C.L. Lucero, R.P. Spragg, D.P. Bentz, D.S. Hussey, D.L. Jacobson, W.J. Weiss, Neutron radiography measurement of salt solution absorption in mortar, *ACI materials journal*, 114 (2017) 149.
- [80] P. Zhang, F. Wittmann, M. Haist, H. Müller, P. Vontobel, T. Zhao, Water penetration into micro-cracks in reinforced concrete, *Restoration of Buildings and Monuments*, 20 (2014) 85-94.

- [81] P. Zhang, F.H. Wittmann, T.-j. Zhao, E.H. Lehmann, P. Vontobel, Neutron radiography, a powerful method to determine time-dependent moisture distributions in concrete, *Nuclear Engineering and Design*, 241 (2011) 4758-4766.
- [82] P. Zhang, F. Wittmann, T. Zhao, E. Lehmann, L. Tian, P. Vontobel, Observation and quantification of water penetration into strain hardening cement-based composites (SHCC) with multiple cracks by means of neutron radiography, *Nuclear instruments and methods in physics research section A: Accelerators, Spectrometers, Detectors and Associated Equipment*, 620 (2010) 414-420.
- [83] Y. Şahin, Y. Akkaya, F. Boylu, M. Taşdemir, Characterization of air entraining admixtures in concrete using surface tension measurements, *Cement and Concrete Composites*, 82 (2017) 95-104.
- [84] N.S. Martys, C.F. Ferraris, Capillary transport in mortars and concrete, *Cement and concrete research*, 27 (1997) 747-760.
- [85] W. Chen, J. Liu, F. Brue, F. Skoczylas, C.A. Davy, X. Bourbon, J. Talandier, Water retention and gas relative permeability of two industrial concretes, *Cement and Concrete Research*, 42 (2012) 1001-1013.
- [86] F.A. Dullien, *Porous media: fluid transport and pore structure*, Academic press 2012.
- [87] C. Gallé, Effect of drying on cement-based materials pore structure as identified by mercury intrusion porosimetry: a comparative study between oven-, vacuum-, and freeze-drying, *Cement and concrete research*, 31 (2001) 1467-1477.